

# Coherent Spectral Feature Extraction Using Symmetric Autoencoders

Archisman Bhattacharjee, Pawan Bharadwaj

**Abstract**—Hyperspectral data acquired through remote sensing are invaluable for environmental and resource studies. While rich in spectral information, various complexities such as environmental conditions, material properties, and sensor characteristics can cause significant variability even among pixels belonging to the same material class. This variability poses nuisance for accurate land-cover classification and analysis. Focusing on the spectral domain, we propose an autoencoder architecture called the symmetric autoencoder (SymAE), which leverages permutation invariant representation and stochastic regularization in tandem to disentangle class-invariant ‘coherent’ features from variability-causing ‘nuisance’ features on a pixel-by-pixel basis. This disentanglement is achieved through a purely data-driven process, without the need for hand-crafted modeling, noise distribution priors, or reference ‘clean signals’. Additionally, SymAE can generate virtual spectra through manipulations in latent space. Using AVIRIS instrument data, we demonstrate these virtual spectra, offering insights on the disentanglement. Extensive experiments across five benchmark hyperspectral datasets show that coherent features extracted by SymAE can be used to achieve state-of-the-art pixel-based classification. Furthermore, we leverage these coherent features to enhance the performance of some leading spectral-spatial HSI classification methods. Our approach especially shows improvement in scenarios where training and test sets are disjoint, a common challenge in real-world applications where existing methods often struggle to maintain relatively high performance.

**Index Terms**—autoencoders, deep learning, hyperspectral imaging, nuisances, variability, redatuming, virtual images, spectral feature extraction, hyperspectral image classification

## I. INTRODUCTION

Hyperspectral imaging has emerged as a powerful tool in remote sensing, offering detailed spectral information across hundreds of narrow contiguous bands. This rich spectral data enables precise material identification and characterization, crucial for applications ranging from land cover classification to environmental monitoring. In precision agriculture, for instance, it facilitates vegetation analysis for crop health assessment [1], [2], while in geological surveys, it enables mineral identification, enhancing the efficiency of exploration activities [3], [4].

Despite its capabilities, hyperspectral imaging faces challenges due to the complexity of its data. The high dimensionality of hyperspectral data, combined with various sources of spectral variability, introduces uncertainty in land cover classification and other inferential tasks. This variability stems from intrinsic material properties (e.g., intra-class variations in

morphology or surface characteristics, even among nominally identical materials) and extrinsic factors (e.g., spatial heterogeneity within pixels, spectral mixing) [5]. Environmental influences, such as atmospheric conditions and illumination variations, also contribute to these challenges (see Figure 1). Variations in sensor-target-illumination geometry can alter the observed spectra. The variability of noise across different scenes, whether due to instrument characteristics or environmental conditions, adds to the complexity [6], [7]. These sources of variability introduce inconsistencies in the observed spectra, potentially leading to misclassification or erroneous analysis of land cover types. Furthermore, these factors can interact in non-linear ways [8], complicating the development of robust approaches to address them. These interrelated aspects contribute to the multifaceted nature of hyperspectral data, necessitating sophisticated methods for analysis.

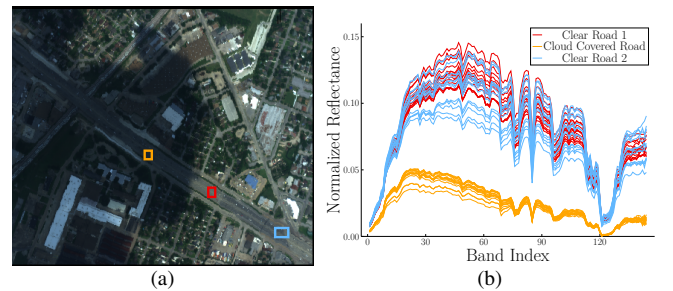


Fig. 1. Demonstration of spectral variability within the road class. (a) False-color image of an urban area with samples from three road segments highlighted: clear road 1 (red), cloud-covered road (orange), and clear road 2 (sky-blue). (b) Normalized reflectance spectra of the highlighted road segments across different spectral bands, illustrating the intra-class variability due to different conditions. This variability complicates precise identification of surface features.

To address these challenges and improve land cover identification performance, we propose using an autoencoder architecture [9], [10], called the Symmetric Autoencoder (SymAE) [11]. Our method focuses on extracting class-invariant spectral features, which we call *coherent features*, disentangled from features representing variability within classes, which we term *nuisance features*, in its latent space. Our approach is based on the following premise:

- For a given spectral class, there exists a subset of spectral characteristics that remain coherent despite various sources of spectral variability, including intrinsic, extrinsic and environmental factors. Isolating these coherent features could enhance spectral classification, as they are potentially more robust to spectral variability.

Traditional autoencoding ideas alone cannot perform this disentangled representation learning. To achieve disentanglement between coherent and nuisance features, we implement the permutation invariance symmetry in our encoder network (detailed in Section III). This symmetry is applied to groups of spectra that share common characteristics, such as those belonging to a specific spectral class, for instance, a particular mineral type, vegetation species, or urban surface material. SymAE enables the generation of virtual spectra through manipulations in latent space. For example, we can extract coherent features from one pixel and nuisance features from another and then decode them to generate a virtual spectrum. In Section IV, we show that these virtual spectra can be used as a sanity check for our coherent feature disentanglement process. Once our encoder is trained to extract coherent features, we use it for classification tasks. We conducted purely spectral classification experiments and also explored integrating these features into leading spectral-spatial HSI classification methods. Section V details these experiments and evaluates the impact of coherent features on classification accuracy in different scenarios.

#### *A brief history of feature extraction approaches*

Addressing the challenges due to spectral variability and improving land cover identification performance has been a focus of research for decades, leading to the development of various feature extraction techniques [12]. Early approaches relied on shallow feature extraction methods such as Principal Component Analysis (PCA), Independent Component Analysis (ICA), and Linear Discriminant Analysis (LDA) to reduce data dimensionality, extract informative features, and enhance class separability [13], [14], [15]. These techniques were often coupled with statistical learning classifiers, such as Support Vector Machines (SVM), for land cover identification [16]. As the field progressed, more sophisticated methods emerged, including manifold learning and kernel-based approaches, which aimed to better capture the non-linear nature of hyperspectral data [17], [18]. The incorporation of spatial information through techniques like Extended Morphological Profiles (EMPs) and Composite Kernel Learning marked a significant advancement, recognizing the importance of spatial context in land cover classification [19], [20].

Since the early 2010s, deep learning methods have gained traction in hyperspectral image analysis, marking a transition from shallow, handcrafted feature extraction to deep, data-driven approaches [21]. This shift has enabled the development of models capable of capturing complex patterns present in hyperspectral data. Unlike previous shallow feature extractors, these deep learning methods often extract features and perform classification in an end-to-end manner. Various architectures have been explored, including Convolutional Neural Networks (CNNs), Stacked Autoencoders (SAEs), Recurrent Neural Networks (RNNs), and Graph Convolutional Networks (GCNs), each addressing different aspects of hyperspectral feature learning [22], [23], [24], [25], [26]. More recently, transformer-based networks have demonstrated high performance, leveraging their sequential understanding and atten-

tion mechanisms to model global spectral-temporal dependencies [27], [28], [29].

Recently, spectral-spatial patch-based deep learning methods have emerged as the state-of-the-art in HSI classification, leveraging both spectral signatures and spatial contexts for improved accuracy. These methods process local neighborhoods to automatically learn robust and discriminative features. Various models have been developed in this category, including residual networks, attention-based models, and approaches integrating transformer architectures with convolutional methods [30], [31], [32], [33], [34], [35], [36]. Recent innovations have also explored optical flow features and spatial relationship modeling to further enhance classification accuracy [37], [38], [39].

#### *Current challenges and our contribution*

Despite significant advancements in feature extraction methods, challenges persist in real-world remote sensing applications. A particular concern is the performance of leading spectral-spatial methods in scenarios where training and test areas are geographically separated, a common situation in practical applications. Our experiments indicate that these methods struggle to relatively maintain their effectiveness under such conditions, highlighting the need for more robust approaches (see Section V-B).

Our approach presents a notable advantage: by training the model to extract coherent features, it demonstrates improved resilience to spectral variability. By leveraging these coherent features, we achieve state-of-the-art purely spectral classification accuracy. Furthermore, our method can complement existing spectral-spatial methods, resulting in performance improvements, notably in scenarios where training and test sets are spatially disjoint, suggesting better generalization to unseen regions.

The remainder of this paper is organized as follows: Section II discusses the spectral grouping process; Section III details the SymAE architecture; Section IV presents insights into the disentanglement process through experiments; Section V describes HSI classification experiments; and Section VI discusses extending our approach to unsupervised grouping, identifies areas for improvement, and outlines future directions before concluding.

## II. SPECTRAL GROUPING AND DATASETS USED

In this section, we discuss the spectral grouping process. The SymAE architecture is designed to disentangle features of data that remain consistent within groups from features that fluctuate within these groups. Consequently, the representations learned by SymAE are fundamentally dependent on how the input data is grouped. To illustrate this concept in the context of hyperspectral imaging, consider an image of an agricultural area. If we group pixels based on crop types (e.g., corn, soybeans, wheat), SymAE would learn to separate features that are common within each group from those that vary. In this scenario, the ‘coherent’ features learned might correspond to the consistent spectral features of each crop type, while the ‘nuisance’ features could capture variations in

appearance caused by factors like soil moisture, plant health, or illumination conditions. Importantly, SymAE performs this separation based solely on the provided grouping, without any prior knowledge of specific crop characteristics or variability factors.

The choice of grouping strategy is therefore crucial, as it directly influences the nature of the features disentangled by SymAE and, consequently, the performance of subsequent analysis tasks. In this study, we explore two types of grouping, leveraging a priori information derived from: 1) ground truth labeling and 2) spatial proximity.

- 1) **Ground Truth Labeling:** Groups are formed based on predefined class labels, such as specific land cover types or material classes identified in the hyperspectral image. Each group contains pixels assigned to the same class. SymAE is then trained to separate spectral features that are coherent within each group from those that vary, potentially corresponding to class-specific spectral signatures and instance-specific variations respectively. A subset of ground-truth labeled pixels is used to train SymAE, while the remaining labeled pixels are reserved for validation and further analysis of the learned features.
- 2) **Spatial Proximity:** In cases where ground truth labels are limited, we group spatially proximate pixels (groups of 9 pixels in  $3 \times 3$  patches). Here, SymAE is trained to extract spatially coherent features. This is an initial approach to explore SymAE’s potential application to fully unsupervised cases where labeled data isn’t available but natural groupings may exist. Section VI-A delves into the preliminary findings and future prospects of unsupervised applications of SymAE.

Our study utilizes five popular hyperspectral datasets, each with distinct characteristics and challenges:

- **Kennedy Space Center (KSC):** Acquired by AVIRIS [40] instrument over Florida, USA. The dataset covers  $512 \times 614$  pixels at 18 m spatial resolution, with 176 spectral bands ranging from 400 to 2500 nm. It includes 13 upland and wetland classes, totaling 5,211 labeled pixels. KSC represents a complex coastal ecosystem with similar vegetation types. KSC serves as our primary dataset for demonstrating virtual spectra generation and analysis.
- **Indian Pines (IP):** Collected using AVIRIS over an agricultural landscape in Indiana, USA. It spans  $145 \times 145$  pixels at 20 m resolution, with 200 spectral channels in the 400-2500 nm range. The dataset contains 16 vegetation classes and 10,249 labeled samples, notably featuring significant class imbalance.
- **Pavia University (PU):** Captured by ROSIS [41] sensor over Pavia, Italy, representing an urban environment. It covers  $610 \times 340$  pixels at 1.3 m/pixel resolution, with 103 spectral bands between 430-860 nm. UP includes 9 urban land cover types, comprising 42,776 labeled pixels.
- **Pavia Center (PC):** Captured by the ROSIS sensor over Pavia, Italy, this dataset represents an urban environment with nine distinct land cover types. The image used in our study measures  $1096 \times 715$  pixels, with a spatial

resolution of 1.3 meters per pixel and includes 102 spectral bands. From the original 148,152 labeled pixels, we selected a subset of 19,800 to create disjoint and balanced train-test sets for the experiments.

- **Houston 2013 (UH):** Acquired by CASI-1500 sensor over the University of Houston campus and surrounding area. The dataset spans  $349 \times 1905$  pixels at 2.5 m resolution, with 144 spectral bands ranging from 364 to 1046 nm. It features 15 urban classes with 15,029 labeled pixels, and uniquely offers spatially disjoint training and testing subsets.

### III. SYMMETRIC AUTOENCODER

SymAE is a data-driven deep learning architecture designed to disentangle coherent features from nuisance variations in grouped datasets where multiple instances share common underlying information but differ due to variable factors. SymAE achieves this separation through a combination of permutation invariance and stochastic regularization, without requiring explicit physical models or labeled data. In their introductory paper [11], Bharadwaj et al. demonstrated SymAE’s application in geophysical settings, particularly for redatuming [42], [43] seismic data to isolate subsurface information from source-related variations. This approach showed promise in handling complex, multi-instance data with unmodeled variability.

In this paper, we adapt SymAE for application in hyperspectral imaging, where the goal is to separate consistent spectral characteristics of different materials or land cover types from various sources of spectral variability.

#### 3.1 Problem Formulation

In the context of HSI, we formulate each pixel spectrum as a function of two components:

- 1) **Coherent features ( $C$ ):** Latent features representing spectral characteristics that are consistent within the group the pixel belongs to.
- 2) **Nuisance features ( $N$ ):** Pixel-specific latent representation of features representing variability factors that cause individual pixels to deviate from the group’s shared characteristics.

Mathematically, we can express a pixel spectrum  $P$  as:

$$P = f(C, N)$$

where  $f$  is an unknown function combining coherent and nuisance features. Notably,  $C$  is shared within a group while  $N$  can vary for each pixel. The goal of SymAE is to learn:

- 1) Encoding functions that collectively approximate the inverse of  $f$ , separating  $P$  into  $C$  and  $N$ .
- 2) A decoding function that approximates  $f$ , reconstructing  $P$  from  $C$  and  $N$ .

#### 3.2 Data Structure

The basic data structure that SymAE operates on is a collection of pixels belonging to the same group, which we

call a datapoint  $X$ . A datapoint  $X$  is formed by stacking  $n_\tau$  pixel spectra from the same group:

$$X = \begin{bmatrix} P_1 \\ P_2 \\ \vdots \\ P_{n_\tau} \end{bmatrix} = \begin{bmatrix} X[1] \\ X[2] \\ \vdots \\ X[n_\tau] \end{bmatrix}$$

where  $P_i$  represents the  $i$ -th pixel spectrum in the datapoint. Each  $P_i$  is a vector of length  $n_{\text{band}}$ , equal to the number of spectral bands. In later parts of this section, we express the  $i$ -th pixel of datapoint  $X$  as  $X[i]$ , which corresponds to  $P_i$ . This structure allows SymAE to learn coherent features shared within each group while capturing pixel-specific nuisances. During training, datapoints are repeatedly generated for each group by sampling  $n_\tau$  pixels with replacement from that group, ensuring diverse representations of group characteristics across different iterations while maintaining within-datapoint coherence.

TABLE I  
Summary of Key Mathematical Notations

Notation	Description	Dimension/Quantity
<i>Data Representation</i>		
$P$	Individual pixel spectrum	$\mathbb{R}^{n_{\text{band}}}$
$X$	Datapoint: collection of $n_\tau$ pixel spectra from the same group	$\mathbb{R}^{n_\tau \times n_{\text{band}}}$
$X[i]$	$i$ -th pixel spectrum in datapoint $X$	$\mathbb{R}^{n_{\text{band}}}$
$n_\tau$	Number of pixel spectra in a datapoint	Scalar, $n_\tau \in \mathbb{N}$
$n_{\text{band}}$	Number of spectral bands	Scalar, $n_{\text{band}} \in \mathbb{N}$
<i>Feature Representation</i>		
$C$	Coherent features: consistent spectral characteristics within a group	$\mathbb{R}^{d_c}$
$N$	Nuisance features: pixel-specific variability	$\mathbb{R}^{d_n}$
<i>SymAE Architecture</i>		
$\text{CEnc}$	Coherent Encoder: Designed to extract coherent features from pixels	$\text{CEnc} : \mathbb{R}^{n_{\text{band}}} \rightarrow \mathbb{R}^{d_c}$
$\text{CEnc}_{\text{mean}}$	Applies $\text{CEnc}$ to datapoints to create permutation-invariant features	$\text{CEnc}_{\text{mean}} : \mathbb{R}^{n_\tau \times n_{\text{band}}} \rightarrow \mathbb{R}^{d_c}$
$\text{NEnc}$	Nuisance Encoder: Designed to extract pixel-specific nuisance features	$\text{NEnc} : \mathbb{R}^{n_{\text{band}}} \rightarrow \mathbb{R}^{d_n}$
$\text{Dec}$	Decoder: Reconstructs pixel spectra from coherent and nuisance features	$\text{Dec} : \mathbb{R}^{d_c} \times \mathbb{R}^{d_n} \rightarrow \mathbb{R}^{n_{\text{band}}}$
$d_c$	Dimension of the coherent code	Scalar, $d_c \in \mathbb{N}$
$d_n$	Dimension of the nuisance code	Scalar, $d_n \in \mathbb{N}$
<i>Training and Evaluation</i>		
$\hat{X}$	Reconstructed datapoint	$\mathbb{R}^{n_\tau \times n_{\text{band}}}$
$L$	Expected reconstruction error	Scalar, $L \in \mathbb{R}_{\geq 0}$

### 3.3 SymAE Architecture

SymAE comprises three main functions parameterized by dense feed-forward networks:

- **Coherent Encoder (CEnc):** Extracts coherent features. Maps each input spectrum  $X[i] \in \mathbb{R}^{n_{\text{band}}}$  to an intermediate feature space  $\mathbb{R}^{d_c}$ , where  $d_c$  is the dimension of the coherent code.
- **Nuisance Encoder (NEnc):** Captures pixel-specific nuisance variations. Maps each input spectrum  $X[i] \in \mathbb{R}^{n_{\text{band}}}$  to a nuisance feature space  $\mathbb{R}^{d_n}$ , where  $d_n$  is the dimension of the nuisance code.
- **Decoder (Dec):** Reconstructs the input spectra using both coherent and nuisance features. Maps a combined vector  $[C, N[i]] \in \mathbb{R}^{d_c + d_n}$  to reconstruct an input spectrum  $\hat{X}[i] \in \mathbb{R}^{n_{\text{band}}}$ .

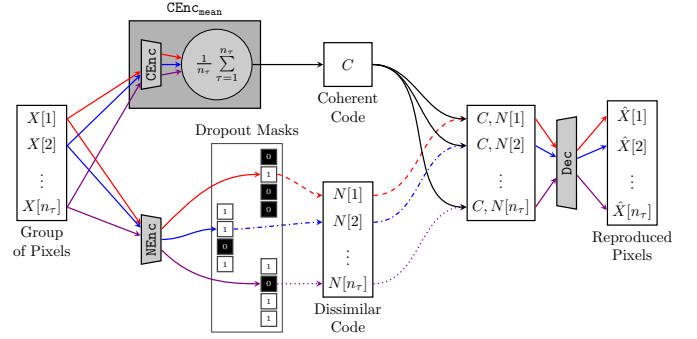


Fig. 2. The architecture of symmetric autoencoder (SymAE) disentangles coherent features from features representing variability in its latent space. The coherent features are assumed to be consistent across the pixels in a group. They propagate through the network via solid black arrows, extracted by a symmetric function ( $\text{CEnc}_{\text{mean}}$ ) that is invariant to pixel ordering. Colored arrows indicate the propagation of pixel-specific nuisance effects, processed by the nuisance encoder (NEnc). Dropout masks are applied to the nuisance features to introduce stochastic regularization. The decoder (Dec) combines coherent and nuisance features to reconstruct pixel spectra.

The processing of an input datapoint  $X$  through SymAE involves two encoding paths, as illustrated in Figure 2. The encoded features are combined in the latent space and subsequently decoded through Dec to reconstruct  $X$ . The first path, via  $\text{CEnc}_{\text{mean}}$ , extracts coherent features shared across pixels in  $X$ . To ensure this path encodes only shared features, we impose an invariance constraint. Specifically, for any permutation  $\Pi$  of the pixel ordering:

$$C = \text{CEnc}_{\text{mean}}(X) = \text{CEnc}_{\text{mean}}(X[\Pi(1:n_\tau)]) \quad (1)$$

This constraint guarantees that the extracted features  $C$  are independent of pixel ordering, thus focusing on characteristics shared across the entire datapoint  $X$ . Consequently, nuisance effects, which differ across pixels, cannot be encoded using  $\text{CEnc}$  without significant information loss. SymAE's coherent encoder achieves the aforementioned invariance using permutation-invariant network architectures, following the approach in [44]. These architectures provide universal approximation guarantees for symmetric functions, typically employing pooling operations such as *mean* or *max* across instances to ensure permutation invariance. In our implementation, the spectrum of each pixel is transformed using  $\text{CEnc}$ , and the mean is taken along the pixel dimension:

$$C = \text{CEnc}_{\text{mean}}(X) = \left( \frac{1}{n_\tau} \sum_{\tau=1}^{n_\tau} \text{CEnc}(X[\tau]) \right) \quad (2)$$

The key aspect of this equation is that the mean of the transformed instances  $\text{CEnc}(X[\tau])$  is symmetric with respect to the ordering of pixels, thereby ensuring the desired symmetry (eqn. 1) is achieved.

The second encoding path in SymAE captures pixel-specific deviations for each pixel of the datapoint  $X$ . In this path, the datapoint passes through the nuisance encoder  $\text{NEnc}$ , which, unlike  $\text{CEnc}$ 's path, is unconstrained. This lack of constraints on  $\text{NEnc}$  presents a significant concern: the decoder Dec might tend to ignore the coherent component  $C$  in favor of only using information from  $N$  for reconstruction. As



the purpose of NEnc is exclusively to encode pixel-specific nuisance information while disregarding coherent features, SymAE incorporates stochastic regularization to mitigate this issue. This regularization is implemented through dropout masks during training, utilizing Bernoulli dropout [45] with a probability of  $p = 0.5$ :

$$N[\tau] = \text{Dropout}(\text{NEnc}(X[\tau])) \quad (3)$$

The dropout mechanism introduces random obfuscation to elements of  $N$ , causing the decoder Dec to perceive the codes as dissimilar and hindering the reconstruction of coherent information from  $N$ . This process creates a dichotomy in the information flow:

- 1) A continuous stream of information from CEnc
- 2) Outputs from NEnc with randomly obfuscated features

This dichotomy compels Dec to extract maximal meaningful information from  $C$ , which inherently contains coherent data. Consequently, the architecture evolves such that:

- Dec becomes adept at capturing coherent information from CEnc
- The remaining pixel-specific features are encoded by NEnc and learned from  $N$

This design of SymAE allows for the simultaneous learning of coherent and nuisance features without prior knowledge of their specific characteristics or distributions.

### 3.4 Training Process

SymAE employs end-to-end training, simultaneously optimizing NEnc, CEnc, and Dec. The training process revolves around reconstructing the input datapoints using the extracted coherent and nuisance features. The decoder combines the coherent code  $C$  with each pixel's nuisance code  $N[\tau]$  to reconstruct the original pixel spectra:

$$\hat{X}[\tau] = \text{Dec}([C, N[\tau]]) \quad \text{for } \tau = 1 \text{ to } n_\tau,$$

where  $\hat{X}[\tau]$  is the reconstructed spectrum for the  $\tau$ -th pixel in the datapoint. The model is trained by minimizing the reconstruction error:

$$L = \frac{1}{n_X} \sum_{i=1}^{n_X} \|X_i - \hat{X}_i\|^2, \quad (4)$$

where  $X_i$  is an input datapoint,  $\hat{X}_i$  is its full reconstruction, and  $n_X$  denotes the total number of datapoints.

It's important to note that while dropout is applied to the nuisance codes during training, at inference time, the full  $N[\tau]$  code is used without dropout. Effective training of SymAE requires datapoints with diverse pixel-specific variations. This diversity is crucial for learning a robust representation in the latent space, where coherent and nuisance features are effectively separated.

### 3.5 Feature Extraction and Virtual Spectra Generation

Post-training, SymAE's encoding functions can be applied to individual pixel spectra for feature extraction. For a given pixel spectrum  $P$ , we can obtain:

- 1) Coherent features:  $C = \text{CEnc}(P)$

- 2) Nuisance features:  $N = \text{NEnc}(P)$

Note that during feature extraction, the full NEnc output is used without dropout. These extracted features can be used to generate virtual spectra through manipulations in the latent space. A basic formulation for this process is:

$$P_{\text{virtual}} = \text{Dec}([C_i, N_j]) \quad (5)$$

where  $C_i$  and  $N_j$  are coherent and nuisance features that may come from different pixels. This capability allows for the creation of hypothetical spectral signatures by combining features from various sources.

## IV. DISENTANGLEMENT VIA SYMAE: ANALYSIS ON KSC DATASET

This section examines SymAE's feature extraction capabilities using the Kennedy Space Center (KSC) hyperspectral dataset. Through experiments on virtual spectra generation and latent space properties, we provide insights into the model's disentanglement process. This analysis serves as a sanity check for our approach, visualizing how SymAE separates class-specific information from instance-specific variations in spectral data.

### A. Experimental Setup

The KSC dataset, acquired by NASA's AVIRIS [40] instrument on March 23, 1996, comprises 13 classes representing various upland and wetland land cover types, with a total of 5,211 labeled pixels. The hyperspectral image had been pre-processed to apparent surface reflectances using the ATREM program [46], which applies atmospheric corrections. A notable characteristic of this dataset is the presence of spectrally similar classes, particularly among vegetation types, which poses challenges for class discrimination using conventional spectral analysis methods. This spectral proximity makes the KSC dataset a relevant testbed for evaluating feature extraction methods.

For our experimental evaluation, we employed a 1 : 9 train-test split ratio of the labeled pixels. The SymAE model was trained on datapoints consisting of  $n_\tau = 8$  pixel spectra, grouped according to their respective ground truth categories. The training process was conducted for 3000 epochs, with each epoch comprising 2048 batches and a batch size of 256. We set the dimensions of both the coherent ( $d_c$ ) and nuisance ( $d_n$ ) latent codes to 64. Our experiments were performed using the Flux machine learning package [47] in Julia programming language. A Linux workstation with 128 GB of RAM, an AMD Ryzen Threadripper 3960X 24-core processor, and a 24 GB NVIDIA GeForce RTX 3090 GPU was used for all computations.

### B. Virtual Spectra and Redatuming

As formulated in Eq. 5, SymAE enables the generation of virtual spectra by combining coherent and nuisance codes from different pixels. In the context of HSI, we introduce *redatuming*, a term borrowed from seismic imaging terminology [42], [11], to describe the process of creating spectra with uniform

nuisance conditions. In this context, redatuming involves generating multiple spectra using consistent nuisance codes while varying the coherent codes, based on the network’s learned separation of these features. Using Eq. 5, we generated virtual spectra with randomly selected reference pixels.

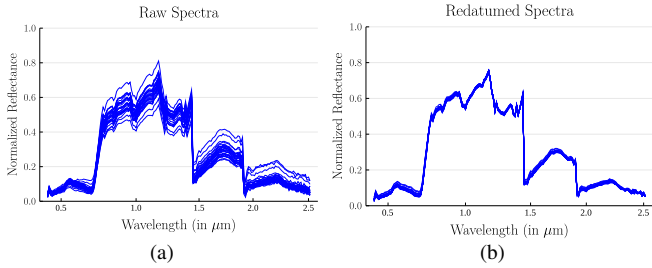


Fig. 3. Redatuming effect on Oak Hammock test spectra. (a) Original spectra with natural variability. (b) Virtual spectra generated by SymAE using a single, consistent nuisance code. Note the reduced variability in (b) while class-specific features are maintained.

Figures 3 and 4 illustrate the resulting reduction in intra-class variance among vegetation spectra. This redatuming effect, achieved by applying consistent nuisance features, extends to test pixels excluded during training while preserving subtle inter-class differences. To quantify intra-class variability, we define *average variance* as the mean of per-band variances within a ground truth class. Table II presents average variance values before and after redatuming with a random pixel. Post-redatuming, the residual average variance in test pixels falls below 5% for most classes, demonstrating significant reduction in intra-class variability.

To examine the effects of redatuming on classification performance, we applied three common classifiers—K-Nearest Neighbors (KNN,  $K=5$ ), Random Forests, and linear Support Vector Machines (SVM)—to both the raw hyperspectral spectra and the virtual spectra generated through redatuming with 1000 different reference pixels. Table III summarizes the overall accuracy (OA) for each classifier.

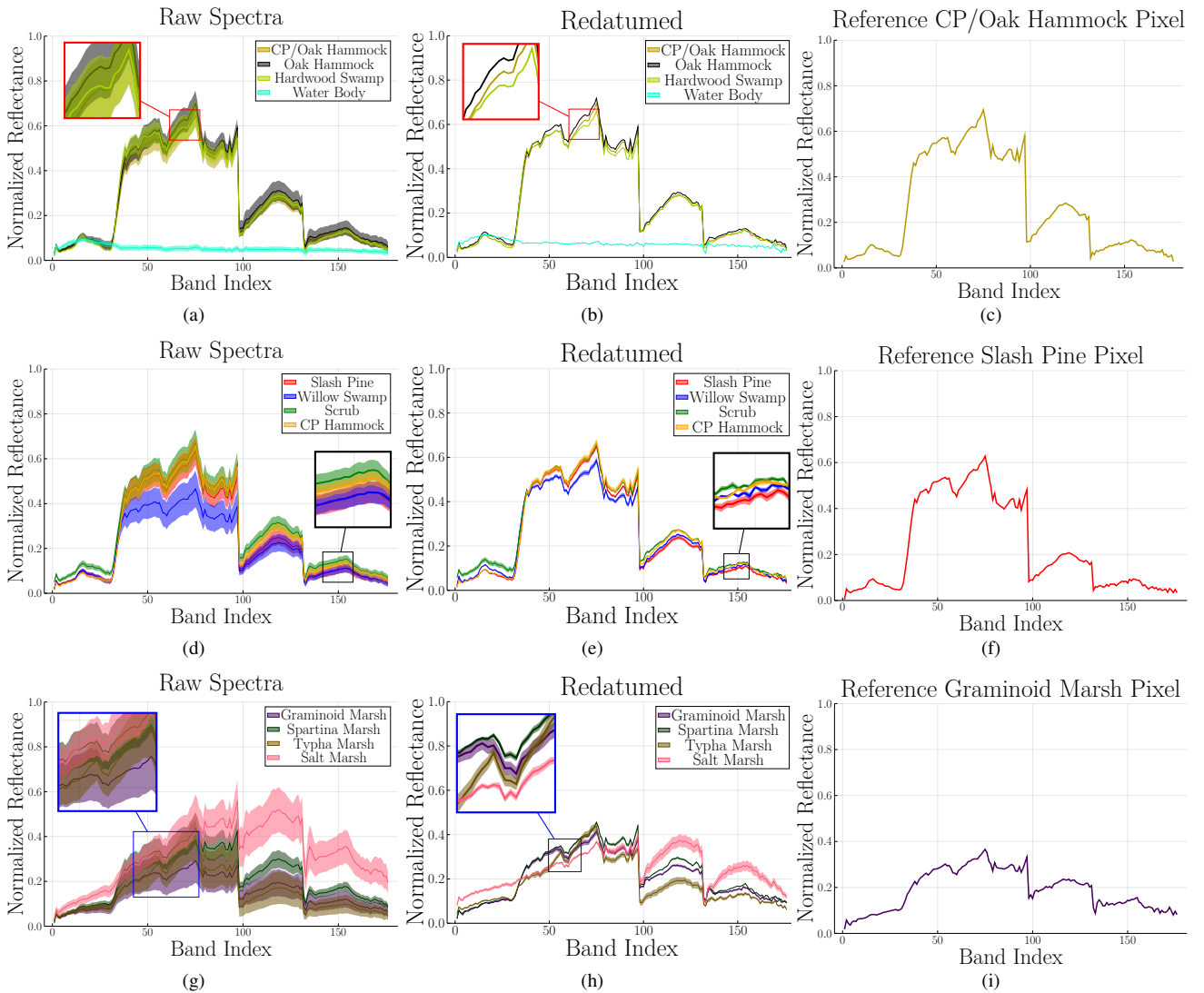


Fig. 4. Ribbon plots illustrate reduction in intra-class variance post-redatuming. Each ribbon plot represents spectral distribution of distinct classes, with central line denoting mean and ribbon’s width on either side indicating intra-class standard deviation. (a) Displays train set spectra from four distinct classes, while (b) shows their respective redatumed counterparts, wherein pixels from the same classes almost coincide, and (c) shows the reference pixel used for redatuming. (d)-(f) Show spectra from test set upland vegetation classes, following the pattern observed in (a)-(c). While not as pronounced as in (b), the redatumed test set pixels exhibit a discernible reduction in intra-class variance. (g)-(i) are same as (d)-(f) but for wetland classes.

TABLE II  
Redatuming Significantly Reduces the Average Variance in Testing Pixels Across Diverse Ground Truth Classes in the KSC Dataset.

No.	Class	Training Samples	Test Samples	Average Variance In Raw Spectra ( $\times 10^{-6}$ )	Average Variance After Redatuming ( $\times 10^{-6}$ )	Residual Variance (%) After Redatuming
1	Scrub	77	684	1173.9	24.6	2.10 %
2	Willow Swamp	25	218	1938.3	17.0	0.88 %
3	CP Hammock	26	230	591.9	38.0	6.42 %
4	CP/Oak Hammock	26	226	1267.6	43.5	3.43 %
5	Slash Pine	17	144	1315.4	22.2	1.69 %
6	Oak Hammock	23	206	1346.5	61.5	4.57 %
7	Hardwood Swamp	11	94	695.3	9.4	1.35 %
8	Graminoid Marsh	44	387	3466.7	51.0	1.47 %
9	Spartina Marsh	52	468	1530.9	132.3	8.64 %
10	Typha Marsh	38	366	3086.0	141.1	4.57 %
11	Salt Marsh	42	377	3986.9	415.4	10.42 %
12	Mud Flats	47	456	1529.5	325.1	21.26 %
13	Water Body	91	836	143.0	0.047	0.03 %

TABLE III  
Classification Accuracy Comparison

Classifier	Raw Spectra OA (%)	Virtual Spectra OA (%)
KNN (K=5)	81.6 %	92.8 $\pm$ 0.9 %
Random Forests	86.2 %	93.0 $\pm$ 0.9 %
Linear SVM	74.0 %	85.8 $\pm$ 4.9 %

The results show improvements in classification accuracy across all methods using virtual spectra generated through redatuming. While KNN and Random Forests demonstrate relatively consistent performance improvements, the linear SVM shows the largest gain in mean accuracy, albeit with higher variability. This sensitivity of the linear SVM, a simpler model, to the choice of reference pixel highlights the importance of reference pixel selection in the redatuming process.

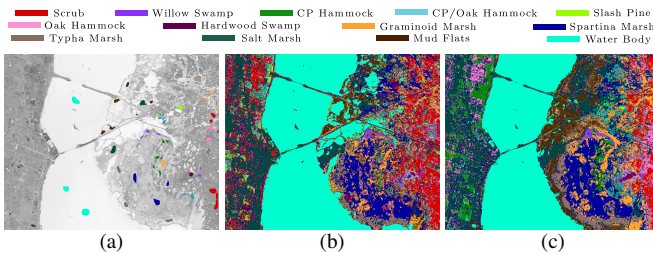


Fig. 5. K-Nearest Neighbors (KNN) pixel classification results on KSC scene maps. (a) Ground truth map of the KSC scene, serving as the baseline. (b) Pixel-wise classification using KNN on the raw image, resulting in an overall accuracy of 81.6% for the test set ground truth. (c) Pixel-wise classification conducted on a virtual image with uniformized nuisance, generated via the redatuming process, which elevated classification performance to an average overall accuracy of 92.8%.

All these observations align with the expected behavior of a disentanglement process, where class-specific information is separated from instance-specific variations. Section V builds on these findings, presenting an approach that uses only the coherent features extracted by SymAE for classification tasks, thus avoiding the need for reference pixel selection.

### C. Distinction from Denoising and Unmixing

SymAE’s approach to hyperspectral data analysis fundamentally differs from traditional unmixing and denoising tasks. Unmixing decomposes mixed pixel spectra into endmember abundances [48], [49], [50], while denoising estimates noise-free spectra [51]. In contrast, SymAE uses abstract representation learning to capture underlying coherent and variable patterns in grouped spectral data. As a result, direct comparisons

between SymAE and these methods are not straightforward. Instead, SymAE provides a complementary perspective, potentially revealing patterns that traditional methods may overlook.

The key distinctions in the features extracted by SymAE are as follows:

- SymAE learns abstract representations that may not directly correspond to physically interpretable spectra.
- Coherent features represent consistent patterns across groups of pixels but do not necessarily equate to ‘pure’ or ‘clean’ spectra.
- Nuisance features capture pixel-specific variations, which differ from traditional notions of ‘noise’ or ‘impurities’.
- Reconstructing a virtual spectrum requires combining both coherent and nuisance features, unlike the clear-cut separation of signal and noise in denoising or the endmember-abundance model in unmixing.

To illustrate these distinctions, we compared SymAE’s performance with a deep learning-based denoising method,

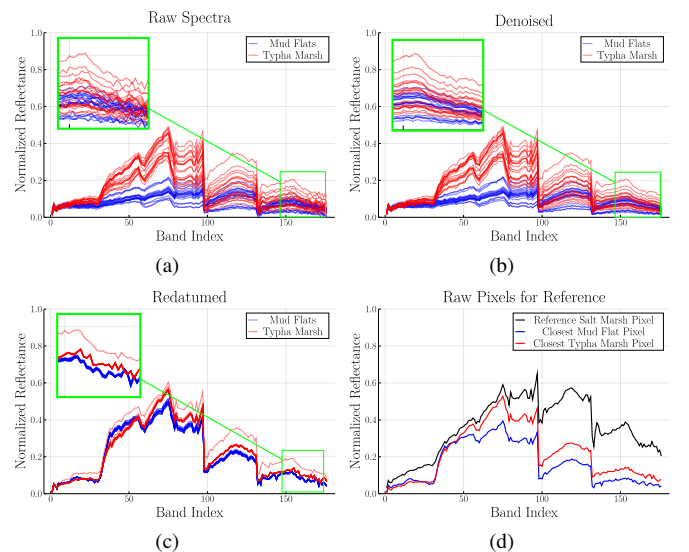


Fig. 6. Comparative analysis of the application of DAE and SymAE on test data. (a) Raw spectra from two land-cover classes in the KSC scene. (b) DAE tends to smooth spectral data, but significant within-group variations remain. (c) Redatuming with SymAE more effectively reduces intra-class variance than denoising with DAE, though the redatumed spectra may differ considerably from the original raw spectra, in this case, exhibiting elevated energy levels. (d) Reference Salt Marsh pixel (with relatively high energy) used for redatuming, along with the real pixels from the respective ground truth classes that are closest to the redatumed spectra.

specifically Denoising Autoencoders (DAEs) [52], [53]. Our experiments show that DAEs smooth spectral data but do not significantly reduce intra-class variance (Fig. 6(b)). In contrast, SymAE’s redatuming more effectively mitigates intra-class variance (Fig. 6(c)). However, unlike conventional denoising techniques, the redatumed spectra may differ noticeably from the raw spectra, retaining influence from the reference pixel used in redatuming (Fig. 6(d)). Additionally, we compared SymAE with sparse unmixing [54] for spectral extraction and subsequent classification. Sparse unmixing achieved 83.14% accuracy on the test set, while using SymAE’s redatuming yielded significantly higher accuracies (see Table III).

Redatuming transforms spectral data in a more complex manner than simple denoising or unmixing. However, its abstract transformation can be challenging to interpret, especially since the choice of reference pixel heavily influences the redatumed virtual spectra. Interpretation may become difficult or nonsensical if the reference pixel belongs to a class with very different characteristics than the pixel being redatumed. For example, marsh classes may exhibit greater spectral variations due to surface water content than upland vegetation classes, while features related to crop ripeness may be irrelevant for water bodies. A detailed physical interpretation of the virtual spectra is beyond the scope of this study, but we discuss the challenges and future directions for more interpretable feature extraction in Section VI. Therefore, the focus of this paper is on leveraging the coherent features for improved land cover or material identification.

#### D. Clustering Analysis of Coherent Features

We designed the coherent features,  $\text{CEnc}(P)$ , to capture consistent spectral characteristics while being robust to variability. To investigate whether these features improve discriminative power, we compare their performance against the original feature space. Our evaluation method involves applying K-means clustering to both the original and coherent feature spaces of the test set. We then assess how well the resulting clusters align with the known class labels, providing a measure of each space’s ability to naturally separate classes.

Our analysis focuses on pairs of classes that are known to be challenging to distinguish in hyperspectral imagery. We initially examined two pairs of spectrally similar classes: Slash Pine vs. Oak Hammock, and CP Hammock vs. CP/Oak Hammock. For each pair, we sampled 100 pixels per class and applied K-means clustering in both the raw spectral space and the coherent feature space.

For Slash Pine and Oak Hammock, K-means clustering in the raw spectral space achieved an accuracy of 75.5%, while in the coherent feature space, it reached 95.9% - a substantial improvement of 20.4 percentage points. Figure 7(a) shows the raw spectra of these classes, while Figure 7(b) illustrates their overlap in the first two principal components of the raw spectral space. In contrast, Figure 7(c) depicts the same pixels projected onto a 2-D linear subspace of the coherent feature space, where improved separation is visually apparent.

The improvement was even more pronounced for the challenging pair of CP Hammock and CP/Oak Hammock (Figures

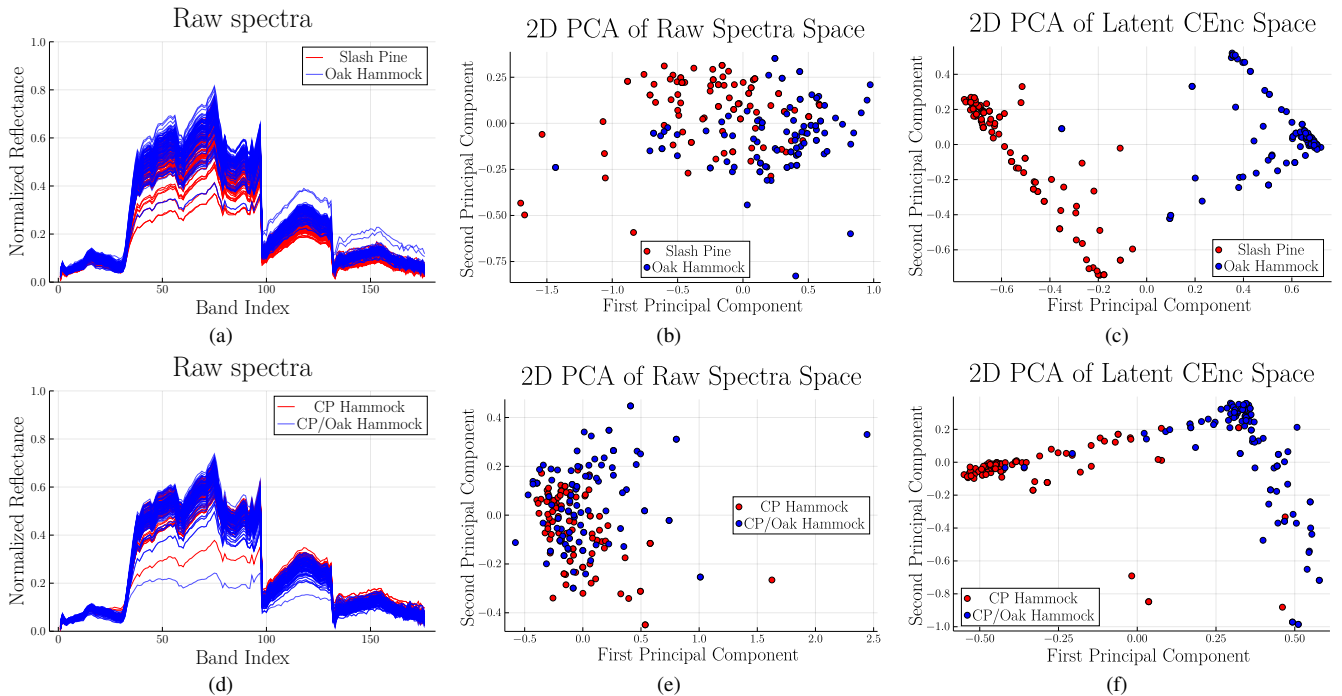


Fig. 7. SymAE extracts coherent features that enhance class separability, particularly for spectrally similar classes. (a,d) Raw spectra of spectrally close-by classes. (b,e) These classes are difficult to separate in 2D raw spectra space. (c,f) The classes with subtle differences in raw spectra are more easily discriminated in the latent coherent code space. The most significant improvement in the K-means clustering experiment is observed for classes with subtle differences, such as CP Hammock and CP/Oak Hammock depicted in (d), (e), and (f).



1	0.0	11.9	45.8	41.1	22.6	37.7	39.9	2.4	6.9	4.7	4.6	0.4	0.2
2	11.9	0.0	12.2	15.9	21.7	11.9	5.9	19.6	32.4	20.9	5.2	3.3	0.4
3	45.8	12.2	0.0	36.3	23.2	42.2	44.6	0.9	2.8	3.9	3.6	0.2	0.0
4	41.1	15.9	36.3	0.0	14.9	32.2	45.1	0.6	3.8	4.5	4.4	0.5	0.7
5	22.6	21.7	23.2	14.9	0.0	20.4	28.0	1.9	3.3	5.4	3.6	0.4	0.0
6	37.7	11.9	42.2	32.2	20.4	0.0	34.3	1.1	4.9	2.7	1.0	0.1	0.0
7	39.9	5.9	44.6	45.1	28.0	34.3	0.0	1.3	1.3	2.6	1.3	0.0	0.0
8	2.4	19.6	0.9	0.6	1.9	1.1	1.3	0.0	21.3	46.0	4.7	24.2	11.7
9	6.9	32.4	2.8	3.8	3.3	4.9	1.3	21.3	0.0	17.5	6.5	2.3	0.0
10	4.7	20.9	3.9	4.5	5.4	2.7	2.6	46.0	17.5	0.0	5.2	22.3	7.9
11	4.6	5.2	3.6	4.4	3.6	1.0	1.3	4.7	6.5	5.2	0.0	2.4	1.9
12	0.4	3.3	0.2	0.5	0.4	0.1	0.0	24.2	2.3	22.3	2.4	0.0	16.0
13	0.2	0.4	0.0	0.7	0.0	0.0	0.0	11.7	0.0	7.9	1.9	16.0	0.0
	1	2	3	4	5	6	7	8	9	10	11	12	13

Fig. 8. Heatmap illustrating improvement in clustering in KSC dataset. The matrix elements indicate the percentage accuracy difference between K-means clustering in the latent coherent code,  $C$ , and clustering in the raw spectral data while doing pairwise unsupervised clustering between land-cover classes. The numbers on axes indicate the class indices, following same ordering as in Table II. This heatmap pertains to the ground truth-based training scenario and the clustering was done on test set. Pairs that show minimal improvement are those that already exhibit significant separation in raw spectra.

7(d), 7(e)). In this case, the accuracy in the raw spectral space was only 53.3%, but it increased to 89.9% in the coherent feature space - an improvement of 36.6 percentage points. This substantial enhancement for highly similar classes underscores the discriminative power of the coherent feature space.

We went on to conduct a comprehensive pairwise clustering experiment encompassing all ground truth classes within the scene. On average, we observed a 12.0 percentage point improvement in clustering accuracy across all class pairs when using the coherent feature space. Notably, the most substantial improvements were evident among classes characterized by subtle spectral differences. Figure 8 illustrates these pairwise improvements in a heatmap, where each element represents the percentage point accuracy difference between clustering in the coherent feature space and the raw spectral space. This visualization highlights the consistent enhancement in class separability achieved by SymAE’s coherent features, particularly for spectrally similar classes.

These observations suggest improved discrimination power in the coherent feature space, particularly for spectrally similar classes. We exploit these coherent features for classification tasks in the following section.

## V. HSI CLASSIFICATION EXPERIMENTS

Classification is a fundamental task in remote sensing, enabling the identification and mapping of targets, land cover types, and other relevant features from imagery. In this section, we utilize the coherent features extracted through SymAE for hyperspectral image classification. We first evaluate our approach in a pixel-based classification context, benchmarking it against other state-of-the-art methods. Then, we explore integrating these coherent features with some leading spectral-spatial classification techniques to provide insights into how they can complement these approaches.

### A. Purely Spectral Classification

Spectral features are the primary source of discriminative information in hyperspectral imaging. To evaluate the coherent features extracted by SymAE, we focus on pixel-based

classification, directly assessing the discriminative power of these spectral features.

We compare our method against several established techniques, including XGBoost [55], a leading tree-based model; the Support Vector Classifier (SVC), a widely used machine learning approach [16]; the 1D Convolutional Neural Network (1D-CNN), which captures spectral patterns using deep learning [22]; the Vision Transformer (ViT), which adapts transformer architectures for image data [27]; and SpectralFormer, a recent state-of-the-art transformer-based model specialized for hyperspectral data, as introduced by Hong et al. [28].

To evaluate the effectiveness of the extracted coherent features, we employ two classification strategies: CEnc + SVC and CEnc + Dense. Both strategies utilize the coherent encoder (CEnc) of trained SymAE model to extract features. In the CEnc + SVC strategy, these features are input to an SVC, while in the CEnc + Dense strategy, they are fed into a dense neural network classifier. The parameters and training configurations for the models compared in this study are as follows:

- 1) XGBoost: Implemented with the `xgboost` package<sup>1</sup> using a multi-class objective (`multi:softprob`), a learning rate of 0.1, a maximum depth of 10, and `mlogloss` for evaluation, trained for 100 rounds.
- 2) SVC: Implemented with the `scikit-learn` package<sup>2</sup> using a radial basis function (RBF) kernel, with `gamma` set to ‘scale’, probability estimates enabled, and `C` parameter values varied logarithmically from 0.0001 to 1000.
- 3) 1D-CNN: The model consists of two 1D convolutional layers with 128 and 16 filters, respectively, followed by batch normalization, ReLU activation, and a fully connected layer for classification.
- 4) ViT: An encoder-only architecture with 5 attention blocks. For the PU, Houston, and IP datasets, we used the configuration suggested by Hong et al. [28] in their GitHub implementation<sup>3</sup>. For the KSC dataset, we trained for 3000 epochs with a learning rate of 0.0005 and no weight decay. For the PC dataset, the model was trained for 800 epochs with a learning rate and weight decay of 0.005.
- 5) SpectralFormer: For the KSC dataset, the model was trained for 1000 epochs using 3-band patches, with a learning rate and weight decay of 0.0005. For the PC dataset, it was trained for 600 epochs using 3-band patches, with a learning rate and weight decay of 0.005. For the other datasets, we followed the configurations suggested by Hong et al. in their GitHub implementation<sup>3</sup>.
- 6) CEnc + SVC: For the KSC and Pavia datasets, the model was trained with  $d_c = d_n = 64$  for 3000 epochs, while for the IP and Houston datasets, it used  $d_c = d_n = 128$  for 4000 epochs. Each training run used 2048 batches of size 256, with  $n_\tau = 8$ . The same SVC configuration as previously mentioned was applied.

<sup>1</sup><https://xgboost.readthedocs.io/en/stable/index.html>

<sup>2</sup><https://scikit-learn.org/stable/modules/generated/sklearn.svm.SVC.html>

<sup>3</sup>[https://github.com/danfenghong/IEEE\\_TGRS\\_SpectralFormer](https://github.com/danfenghong/IEEE_TGRS_SpectralFormer)



TABLE IV  
Pixel-based Classification Results from Kennedy Space Center Dataset.

No.	Class	Training Samples	Test Samples	XGBoost	SVC	1D-CNN	ViT	SpectralFormer	CEnc + SVC	CEnc + Dense
1	Scrub	77	684	95.32%	<b>97.22%</b>	96.05%	92.69%	94.88%	96.49%	95.61%
2	Willow Swamp	25	218	85.32%	88.99%	89.91%	86.70%	88.07%	95.87%	<b>96.79%</b>
3	CP Hammock	26	230	77.39%	87.39%	87.83%	<b>96.09%</b>	87.39%	82.61%	85.22%
4	CP/Oak Hammock	26	226	55.31%	74.78%	69.03%	49.56%	66.37%	<b>82.74%</b>	80.53%
5	Slash Pine	17	144	52.08%	72.92%	62.50%	61.81%	69.44%	75.69%	<b>77.08%</b>
6	Oak Hammock	23	206	43.20%	67.48%	65.53%	42.23%	53.4%	72.33%	<b>77.67%</b>
7	Hardwood Swamp	11	94	64.89%	79.79%	70.21%	76.60%	57.45%	87.23%	<b>88.23%</b>
8	Graminoid Marsh	44	387	84.75%	95.09%	90.44%	85.27%	91.21%	96.12%	<b>96.90%</b>
9	Spartina Marsh	52	468	85.90%	96.37%	97.22%	<b>97.44%</b>	96.79%	97.65%	<b>97.44%</b>
10	Typha Marsh	38	366	89.89%	95.08%	90.98%	95.63%	96.99%	<b>97.54%</b>	97.27%
11	Salt Marsh	42	377	96.55%	<b>98.14%</b>	98.41%	97.88%	96.55%	97.88%	<b>98.14%</b>
12	Mud Flats	47	456	89.04%	97.37%	96.27%	87.06%	94.08%	97.81%	<b>98.90%</b>
13	Water Body	91	836	99.04%	<b>100.0%</b>	<b>100.0%</b>	<b>100.0%</b>	<b>100.0%</b>	<b>100.0%</b>	<b>100.0%</b>
	Overall Accuracy			85.74%	93.03%	91.35%	88.28%	90.49%	94.27%	<b>94.65%</b>
	Average Accuracy			78.36%	88.51%	85.72%	82.23%	84.05%	90.77%	<b>91.53%</b>
	$\kappa \times 100$			84.10	92.23	90.35	86.95	89.40	93.61	<b>94.04</b>

TABLE V  
Pixel-based Classification Results from Indian Pines Dataset.

No.	Class	Training Samples	Test Samples	XGBoost	SVC	1D-CNN	ViT	SpectralFormer	CEnc + SVC	CEnc + Dense
1	Alfalfa	15	31	70.97%	74.19%	77.42%	77.42%	<b>93.55%</b>	90.32%	90.32%
2	Corn-notill	50	1378	47.90%	69.38%	69.09%	60.89%	57.76%	<b>71.34%</b>	68.36%
3	Corn-mintill	50	780	50.90%	69.49%	61.41%	60.51%	<b>70.77%</b>	69.49%	67.82%
4	Corn	50	187	62.57%	78.07%	72.73%	78.61%	82.35%	80.75%	<b>84.49%</b>
5	Grass-pasture	50	433	85.68%	90.99%	84.30%	90.99%	91.69%	<b>92.61%</b>	90.99%
6	Grass-trees	50	680	91.47%	92.50%	92.35%	87.79%	<b>94.12%</b>	92.79%	91.47%
7	Grass-pasture-mowed	15	13	76.92%	84.62%	<b>92.31%</b>	84.62%	84.62%	<b>92.31%</b>	<b>92.31%</b>
8	Hay-windrowed	50	428	93.46%	97.66%	96.03%	96.73%	96.73%	96.73%	<b>97.66%</b>
9	Oats	15	5	40.00%	80.00%	<b>100.0%</b>	80.00%	60.00%	<b>100.0%</b>	<b>100.0%</b>
10	Soybean-no-till	50	922	66.49%	72.67%	70.39%	80.80%	<b>82.00%</b>	77.22%	78.52%
11	Soybean-min-till	50	2405	50.98%	53.14%	46.24%	63.58%	<b>65.03%</b>	62.00%	64.57%
12	Soybean-clean	50	543	47.33%	71.09%	65.38%	63.72%	73.30%	76.06%	<b>78.08%</b>
13	Wheat	50	155	95.48%	<b>99.35%</b>	<b>99.35%</b>	<b>99.35%</b>	98.71%	<b>99.35%</b>	<b>99.35%</b>
14	Woods	50	1215	84.36%	85.02%	86.58%	85.02%	88.07%	89.14%	<b>90.95%</b>
15	Buildings-Grass-Trees-Drives	50	336	53.87%	71.43%	<b>72.02%</b>	50.00%	53.57%	69.64%	70.54%
16	Stone-Steel-Towers	50	43	97.67%	<b>100.0%</b>	<b>97.67%</b>	<b>100.0%</b>	<b>100.0%</b>	97.67%	97.67%
	Overall Accuracy			63.77%	72.50%	69.27%	72.43%	74.94%	76.37%	<b>76.90%</b>
	Average Accuracy			69.75%	80.60%	80.20%	78.75%	80.77%	84.84%	<b>85.20%</b>
	$\kappa \times 100$			59.16	68.98	65.39	68.78	71.62	73.22	<b>73.80</b>

TABLE VI  
Pixel-based Classification Results from Pavia Center Dataset.

No.	Class	Training Samples	Test Samples	XGBoost	SVC	1D-CNN	ViT	SpectralFormer	CEnc + SVC	CEnc + Dense
1	Water	200	2000	96.65%	98.80%	99.50%	99.10%	<b>99.60%</b>	99.35%	99.55%
2	Trees	200	2000	91.25%	93.75%	<b>96.65%</b>	85.45%	88.50%	93.30%	92.85%
3	Asphalt	200	2000	53.90%	76.30%	74.20%	85.25%	<b>91.70%</b>	85.15%	88.50%
4	Self-Blocking Bricks	200	2000	71.70%	77.75%	85.80%	79.45%	<b>86.5%</b>	84.00%	83.60%
5	Bitumen	200	2000	<b>89.95%</b>	89.10%	87.55%	83.80%	83.70%	88.75%	89.00%
6	Tiles	200	2000	87.85%	95.55%	97.50%	94.60%	93.15%	97.80%	<b>97.90%</b>
7	Shadows	200	2000	72.15%	81.25%	<b>81.35%</b>	79.75%	80.05%	80.95%	81.30%
8	Meadows	200	2000	94.90%	97.60%	98.55%	98.50%	98.45%	98.50%	<b>99.10%</b>
9	Bare Soil	200	2000	83.65%	99.80%	99.95%	<b>100.0%</b>	<b>100.0%</b>	<b>100.0%</b>	<b>100.0%</b>
	Overall Accuracy			82.44%	89.99%	91.23%	89.54%	91.29%	91.98%	<b>92.42%</b>
	Average Accuracy			82.44%	89.99%	91.23%	89.54%	91.29%	91.98%	<b>92.42%</b>
	$\kappa \times 100$			80.25	88.74	90.13	88.24	90.21	90.98	<b>91.48</b>

7) CEnc + Dense: The same SymAE models as described in CEnc + SVC were used. A 4-layer dense network with Bernoulli dropout set to 0.5 was employed for classification. The code for training SymAE and the classifier have been made available on github<sup>4</sup>.

The results of the classification experiments on the KSC, PU, PC, IP, and UH datasets are presented in Tables IV, VII, VI, V and VIII respectively. Across all datasets, the CEnc-based methods consistently deliver superior performance, with the best CEnc-based classifier achieving, on average, 2.22 and 2.68 percentage points higher Overall Accuracy (OA) and Average Accuracy (AA), respectively, and a 2.53 point increase in the scaled Kappa coefficient

( $\kappa \times 100$ ), compared to the best method not using CEnc. These improvements support our premise (Premise I, Section I) that isolating coherent features can enhance spectral classification. The results suggest SymAE’s ability to extract features that are more robust to spectral variability compared to the other methods tested in this study.

*Ablation Analysis:* We conducted an ablation study focusing on classes 3-6 from Table IV of the KSC scene, identified as the most challenging to discriminate. For this analysis, all networks underwent training for 4000 epochs, each containing 64 batches with a batch size of 256. Post-training, classification was conducted using latent codes in a similar dense neural network with dropout regularization as previously used. In configurations where both CEnc and NEnc were employed,

<sup>4</sup><https://github.com/archieb1999/SymAE-for-HSI>

TABLE VII  
Pixel-based Classification Results from Pavia University Dataset.

No.	Class	Training Samples	Test Samples	XGBoost	SVC	ID-CNN	ViT	SpectralFormer	CEnc + SVC	CEnc + Dense
1	Asphalt	548	6304	79.93%	84.52%	80.25%	77.19%	87.34%	87.12%	<b>88.06%</b>
2	Meadows	540	18146	57.76%	68.81%	65.31%	67.32%	77.12%	79.58%	<b>79.61%</b>
3	Gravel	392	1815	51.90%	68.98%	69.15%	67.77%	54.93%	69.15%	<b>71.96%</b>
4	Trees	524	2912	<b>98.63%</b>	98.35%	81.63%	95.95%	97.73%	95.05%	94.78%
5	Painted metal sheets	265	1113	99.46%	99.37%	<b>99.64%</b>	99.37%	99.37%	99.55%	<b>99.64%</b>
6	Bare soil	532	4572	83.95%	94.14%	94.27%	89.85%	92.67%	94.75%	<b>96.50%</b>
7	Bitumen	375	981	84.20%	90.32%	87.05%	87.46%	86.14%	<b>91.64%</b>	91.03%
8	Self blocking bricks	514	3364	91.05%	92.42%	86.56%	85.17%	<b>93.73%</b>	91.26%	90.49%
9	Shadows	231	795	97.11%	<b>99.37%</b>	98.62%	97.36%	67.55%	96.35%	98.74%
	Overall Accuracy			72.35%	80.31%	76.28%	77.04%	83.05%	85.32%	<b>85.76%</b>
	Average Accuracy			82.67%	88.48%	84.72%	85.37%	84.06%	89.38%	<b>90.09%</b>
	$\kappa \times 100$			65.64	75.07	70.10	70.99	78.11	80.96	<b>81.53</b>

TABLE VIII  
Pixel-based Classification Results from Houston2013 Dataset.

No.	Class	Training Samples	Test Samples	XGBoost	SVC	ID-CNN	ViT	SpectralFormer	CEnc + SVC	CEnc + Dense
1	Healthy Grass	198	1053	<b>89.74%</b>	83.67%	89.08%	83.76%	86.13%	84.24%	84.05%
2	Stressed Grass	190	1064	97.09%	96.90%	97.37%	97.18%	96.52%	98.59%	<b>98.68%</b>
3	Synthetic Grass	192	505	97.43%	99.80%	99.80%	99.80%	99.80%	99.80%	<b>100.0%</b>
4	Tree	188	1056	94.60%	98.30%	91.76%	<b>98.77%</b>	97.63%	97.54%	96.88%
5	Soil	186	1056	93.94%	97.73%	97.44%	98.01%	<b>98.86%</b>	<b>98.86%</b>	<b>98.86%</b>
6	Water	182	143	96.50%	95.10%	93.71%	<b>98.60%</b>	96.50%	95.10%	<b>98.60%</b>
7	Residential	196	1072	81.53%	83.40%	72.67%	77.52%	<b>86.01%</b>	82.84%	85.35%
8	Commercial	191	1053	49.76%	51.76%	59.92%	56.98%	52.90%	<b>77.97%</b>	60.78%
9	Road	193	1059	68.65%	76.68%	77.71%	67.52%	64.59%	80.64%	<b>82.63%</b>
10	Highway	191	1036	61.10%	81.37%	77.03%	66.70%	93.34%	78.76%	<b>86.20%</b>
11	Railway	181	1054	77.42%	<b>91.37%</b>	84.35%	68.41%	73.15%	87.95%	87.86%
12	Parking Lot1	192	1041	55.33%	68.78%	72.53%	50.82%	58.50%	<b>83.57%</b>	83.38%
13	Parking Lot2	184	285	68.42%	69.12%	70.53%	63.16%	72.98%	77.19%	<b>78.25%</b>
14	Tennis Court	181	247	97.57%	<b>100.0%</b>	98.38%	99.19%	98.79%	98.79%	98.79%
15	Running Track	187	473	95.56%	97.89%	<b>98.73%</b>	98.52%	<b>98.73%</b>	97.46%	97.67%
	Overall Accuracy			79.01%	84.46%	83.59%	78.85%	82.64%	<b>88.14%</b>	87.68%
	Average Accuracy			81.64%	86.12%	85.40%	81.66%	84.96%	<b>89.29%</b>	89.20%
	$\kappa \times 100$			77.28	83.16	82.20	77.10	81.20	<b>87.14</b>	86.62

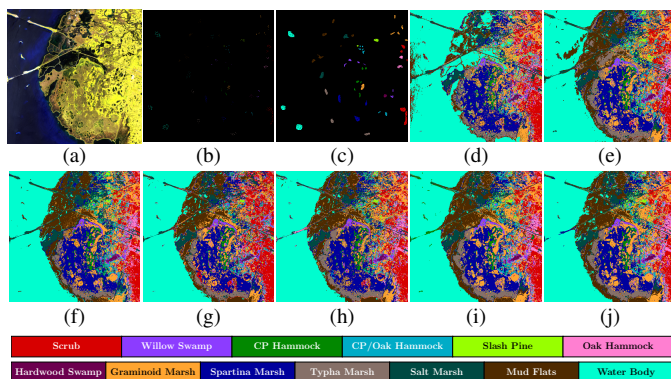


Fig. 9. KSC scene visualization and pixel-based classification maps: (a) False color map, (b) training set, (c) test set, (d) XGBoost, (e) SVC, (f) ID-CNN, (g) ViT, (h) SpectralFormer, (i) CEnc + SVC, (j) CEnc + Dense

the latent code size was equally divided between them. Note that when only NEnc is used, it effectively functions as a stacked autoencoder with stochastic regularization. The results, depicted in Fig. 10, indicate that utilizing both encoders concurrently results in reduced sensitivity to variations in latent code size and consistently yields higher accuracy. This improvement likely stems from the structured disentanglement enforced in SymAE.

### B. Complementing Spectral-Spatial Methods

While our approach using coherent features demonstrated leading performance for a purely spectral method, it is important to acknowledge that state-of-the-art HSI classification

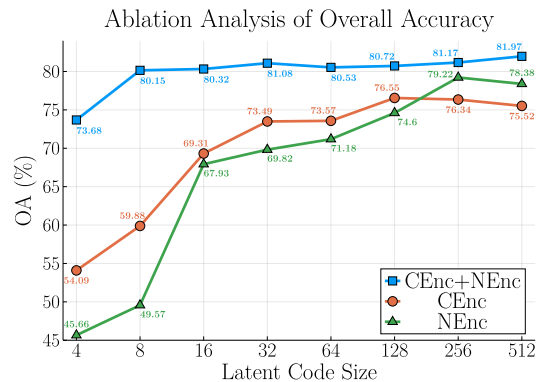


Fig. 10. Ablation study results for classes 3-6 in the KSC scene, showing the impact of using both CEnc and NEnc encoders on classification performance. The results demonstrate reduced sensitivity to latent code size variations and improved accuracy when both encoders are employed concurrently.

methods are predominantly based on spectral-spatial patch-based deep learning techniques. These methods, such as SSRP-net [56], morphFormer [57], SMF-UL [58], and ESSAN [59], leverage local contextual information by capitalizing on the spatial continuity often observed in land cover classes. Consequently, these methods generally exhibit robustness against salt-and-pepper noise, thereby enhancing their accuracy. By incorporating both spectral and spatial information, they have achieved notable performance on benchmark datasets, particularly in cases where classes exhibit high contiguity.

*Limitations of Current Evaluation Practices:* Despite the success of spectral-spatial methods, a critical examination of

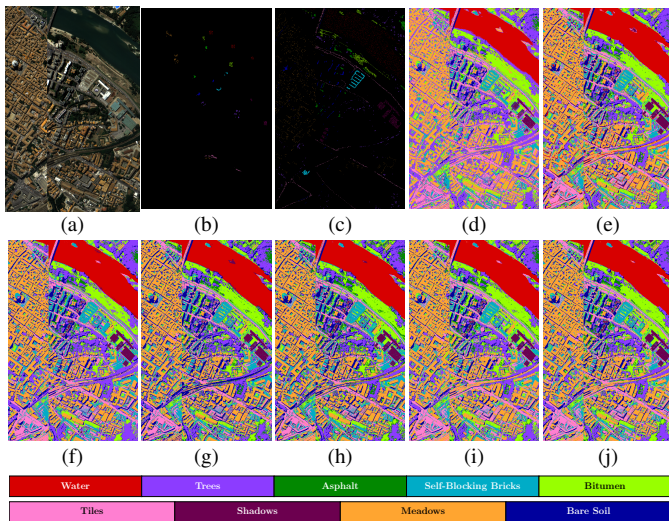


Fig. 11. PC scene visualization and pixel-based classification maps: (a) False color map, (b) training set, (c) test set, (d) XGBoost, (e) SVC, (f) 1D-CNN, (g) ViT, (h) SpectralFormer, (i) CEnc + SVC, (j) CEnc + Dense

common evaluation practices reveals a potential overestimation of their real-world efficacy. Many studies employ random splits between training and test sets without considering spatial adjacency, potentially leading to test pixels being included within training patches. This overlap allows networks to learn the spatial context of test samples. For instance, a  $7 \times 7$  patch centered on a training pixel may inadvertently include neighboring test pixels, providing the model with indirect access to test data during training. This issue can lead to an overestimation of the model’s generalization capabilities, as it does not accurately reflect real-world applications where overlap between training and test areas is typically unlikely, such as in large-scale surveys or when models are applied to novel, unseen regions.

To address these concerns and more accurately assess the practical performance of spectral-spatial methods, we introduce spatially disjoint train-test splits into our evaluation framework, in addition to the typical random splits. This approach allows for a more realistic evaluation of model performance in scenarios where spatial continuity between training and test samples cannot be assumed. In our study, we utilize the following datasets with different split types: the KSC and IP datasets are maintained with spatially random splits for consistency with previous evaluations; the PU dataset is prepared in two versions—one with a spatially random split and another with a largely disjoint split where test samples are contained within rectangular regions (excluding pixels adjacent to region boundaries); the PC dataset uses a subset of the original labeled pixels to create a disjoint and balanced train-test split; and the UH dataset, which includes a pre-defined spatially disjoint train-test split, serving as a benchmark for real-world applicability. The distribution of training and test sets for these scenes can be seen in Figures 9, 12, 13, 14, 11 and 15 respectively.

*Integration of Coherent Features with Spectral-Spatial Methods:* To explore whether our extracted coherent features can enhance existing spectral-spatial methods, we simply

replace the spectral dimension in the hyperspectral data cube with features derived through CEnc. This approach allows us to assess the improvement in spectral information while preserving the models’ ability to leverage spatial context. For this comparative study, we selected four state-of-the-art spectral-spatial models:

- SSTN (Spectral-Spatial Transformer Network) [31]<sup>5</sup>: Utilizes spectral-spatial self-attention to capture long-range dependencies and integrate local and global features.
- FCN (Fully Contextual Network) [34]<sup>6</sup>: Employs scale attention and contextual modules to capture nonlocal spectral-spatial contexts.
- A2S2K-ResNet (Attention-based Adaptive Spectral-Spatial Kernel Improved Residual Network) [33]<sup>7</sup>: Enhances feature selection through selective 3D convolutions and adaptive recalibration.
- AMS-M2ESL (Adaptive Mask Sampling and Manifold to Euclidean Subspace Learning) [39]<sup>8</sup>: Improves spatial modeling via adaptive sampling and manifold-based feature learning.

To ensure consistency in training across all models, we used the same train-test distribution as described in the previous subsection on pixel-based classification. The training split was further divided into an 80-20 train-validation split to standardize the training process and enable best model selection based on validation performance across epochs, as some original implementations included this practice while others did not. We implemented these models using code from their respective authors’ public GitHub repositories<sup>5,6,7,8</sup>, with parameters selected according to recommendations in their papers or repositories. For scenes new to a model (e.g., UH for A2S2K-ResNet), we tested parameters from other scenes and chose the best-performing ones. We evaluated the models both with and without coherent features, maintaining SymAE configurations from the previous subsection. When using coherent features, all other parameters, including patch size, remained consistent with the original implementations, except for AMS-M2ESL, where the MNF ratio parameter was adjusted to 1 for Pavia datasets and 0.4 for others to maintain optimal performance. We evaluated the models both with and without coherent features, maintaining SymAE configurations from the previous subsection. When using coherent features, all other parameters, including patch size, remained consistent with the original implementations, except for AMS-M2ESL, where the MNF ratio parameter was adjusted to 1 for Pavia datasets and 0.4 for others to maintain optimal performance.

The classification results are presented in Table IX. In the KSC and PU datasets with random train-test splits, all models achieved very high accuracies, often exceeding 99%. In these cases, the use of coherent features provided modest improvements due to the already high performance baseline. The IP dataset, despite also having a random split, showed lower overall accuracies compared to KSC and PU, ranging

<sup>5</sup><https://github.com/zilongzhong/SSTN>

<sup>6</sup><https://github.com/DotWang/FullyContNet>

<sup>7</sup><https://github.com/suvojit-0x55aa/A2S2K-ResNet>

<sup>8</sup><https://github.com/lms-07/AMS-M2ESL>



TABLE IX  
Performance Comparison of Spectral-Spatial Methods With and Without Coherent Features Across Multiple Datasets

Dataset	Metric	SSTN	SSTN + CEnc	FCN	FCN + CEnc	A2S2K	A2S2K + CEnc	AMS-M2ESL	AMS-M2ESL + CEnc
Kennedy Space Center <sup>R</sup>	OA (%)	96.12	99.87	98.04	99.68	99.30	99.87	99.64	99.66
	AA (%)	93.02	99.83	96.86	99.45	98.88	99.82	98.82	99.28
	$\kappa \times 100$	95.68	99.86	97.82	99.64	99.22	99.86	99.60	99.62
Indian Pines <sup>R</sup>	OA (%)	88.89	92.85	91.70	93.69	93.80	96.66	93.11	97.18
	AA (%)	94.64	95.40	95.50	96.72	97.51	98.29	97.61	98.63
	$\kappa \times 100$	87.33	91.83	90.49	92.76	92.93	96.17	92.15	96.77
Pavia University <sup>R</sup>	OA (%)	99.31	99.62	99.22	99.43	99.44	99.87	99.61	99.66
	AA (%)	99.09	99.47	99.09	99.22	99.36	99.81	99.61	99.51
	$\kappa \times 100$	99.06	99.48	98.94	99.23	99.24	99.82	99.47	99.53
Pavia University <sup>D</sup>	OA (%)	89.88	94.80	91.73	92.83	89.54	94.34	86.44	93.39
	AA (%)	89.99	96.19	90.02	96.03	92.35	96.86	91.36	96.12
	$\kappa \times 100$	86.50	93.09	88.79	90.57	86.32	92.51	82.39	91.28
Pavia Center <sup>D</sup>	OA (%)	91.14	93.64	82.67	90.30	93.19	94.05	88.03	92.57
	AA (%)	91.14	93.64	82.67	90.30	93.19	94.05	88.03	92.57
	$\kappa \times 100$	90.04	92.84	80.51	89.09	92.34	93.31	86.53	91.64
Houston 2013 <sup>D</sup>	OA (%)	86.11	89.24	78.05	86.97	89.90	91.15	88.42	91.47
	AA (%)	87.85	90.82	76.83	88.18	91.51	92.34	89.48	92.89
	$\kappa \times 100$	84.92	88.31	76.15	85.86	89.03	90.39	87.43	90.73

<sup>R</sup>Spatially Random Train-Test Split, <sup>D</sup>Spatially Disjoint Train-Test Split

from about 89% to 94%. Here, the introduction of coherent features led to more noticeable improvements. Examining the OA improvements in detail, KSC showed improvements ranging from 0.02 to 3.75 percentage points, with SSTN benefiting the most. IP saw more substantial gains, particularly for AMS-M2ESL (4.07) and SSTN (3.96), while PU with random split had minimal improvements, all below 0.5 percentage points. On average, for the datasets with random splits (KSC, IP, and PU), the use of coherent features resulted in improvements of 1.66 and 1.29 percentage points in OA and AA, respectively. The  $\kappa \times 100$  value increased by 1.89 on average.

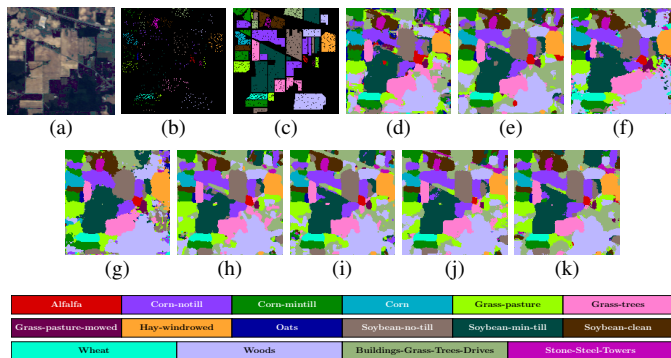


Fig. 12. Classification maps and train-test sets for IP scene: (a) False color map, (b) Train set, (c) Test set, (d) SSTN, (e) SSTN + CEnc, (f) FCN, (g) FCN + CEnc, (h) A2S2K, (i) A2S2K + CEnc, (j) AMS-M2ESL, (k) AMS-M2ESL + CEnc

The most significant impact of coherent features was observed in the datasets with disjoint splits. PU (disjoint) saw notable improvements, especially for AMS-M2ESL (6.95) and SSTN (4.92). PC showed varied improvements, with FCN gaining the most (7.63), while A2S2K saw a modest 0.86 increase. UH demonstrated substantial improvements for FCN (8.92) and SSTN (3.13), with other models showing more moderate gains. Notably, FCN showed the highest variability in improvement, with exceptional gains in PC and UH, but

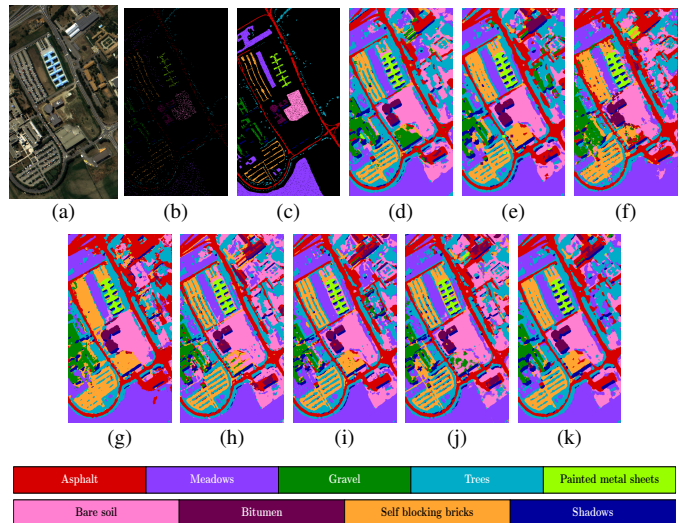


Fig. 13. Classification maps and train-test sets for PU (random-split) scene. (a) False color map, (b) Train set, (c) Test set, (d) SSTN, (e) SSTN + CEnc, (f) FCN, (g) FCN + CEnc, (h) A2S2K, (i) A2S2K + CEnc, (j) AMS-M2ESL, (k) AMS-M2ESL + CEnc

more modest improvements in other datasets. SSTN demonstrated consistent improvements across all datasets, while A2S2K and AMS-M2ESL showed more varied results. For the disjoint cases, the average improvements were substantially higher: 4.14 and 4.63 percentage points in OA and AA, respectively. The  $\kappa \times 100$  value showed an average increase of 4.89. This is a notable increase compared to the random split cases, with improvements more than doubling across all metrics. These results suggest that coherent features have the capability to enhance the performance of spectral-spatial methods, particularly in scenarios where spatial continuity between training and test data is limited. This capability could be beneficial in practical applications where models are applied to novel, unseen regions.

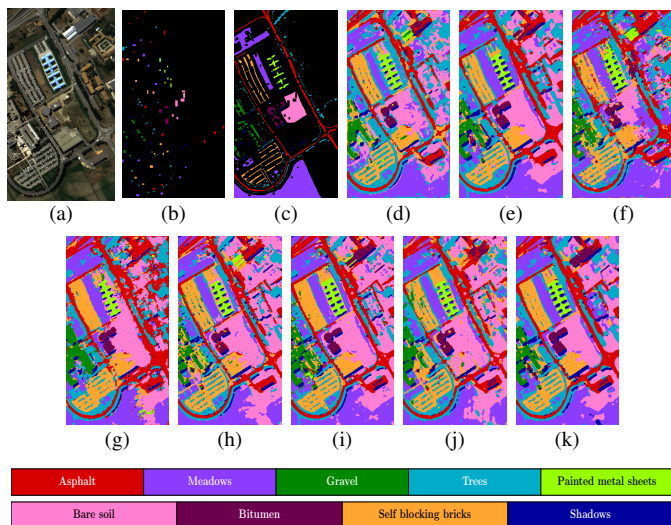


Fig. 14. Classification maps and train-test sets for PU (disjoint) scene. (a) False color map, (b) Train set, (c) Test set, (d) SSTN, (e) SSTN + CEnc, (f) FCN, (g) FCN + CEnc, (h) A2S2K, (i) A2S2K + CEnc, (j) AMS-M2ESL, (k) AMS-M2ESL + CEnc

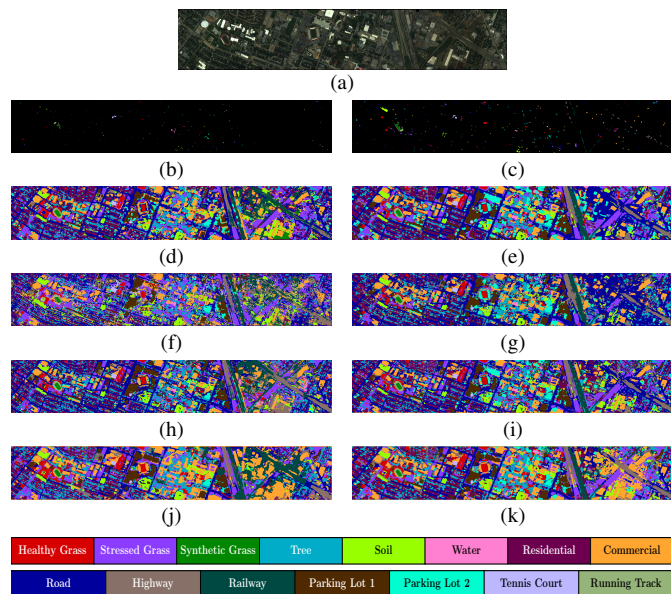


Fig. 15. Classification maps and train-test sets for UH scene. (a) Ground truth, (b) Train set, (c) SSTN, (d) SSTN + CEnc, (e) FCN, (f) FCN + CEnc, (g) A2S2K, (h) A2S2K + CEnc, (i) AMS-M2ESL, (j) AMS-M2ESL + CEnc

## VI. DISCUSSION

This section discusses SymAE’s potential applicability in fully unsupervised settings and identifies areas with scope for improvement and future research.

### A. Unsupervised Grouping

SymAE is designed to train on groups of data, which may naturally occur in many remote sensing applications, even in the absence of ground truth labels. This opens up the possibility of using SymAE in unsupervised settings, where the goal is to extract meaningful features and discover inherent structures in the data without relying on explicit annotations.

Consider, for instance, multi-temporal hyperspectral data in remote sensing applications. In such scenarios, each pixel location might undergo multiple scans under different atmospheric conditions and varying elevation angles. These spectra correspond to the same pixel location but reflect different environmental influences. SymAE aims to disentangle these variations from the pixel-specific reflectance in an entirely unsupervised manner, learning representations that are robust to atmospheric and lighting variations. Another potential example lies in extraterrestrial remote sensing applications. In these environments, sensors may encounter various unmodeled nuisance factors that affect measurements of relatively stable surface compositions. SymAE’s ability to extract coherent features despite these unknown variables could aid in clustering and initial analysis of unexplored regions. This approach may prove valuable in contexts where traditional modeling of environmental factors is challenging or incomplete.

Given the challenges in obtaining suitable datasets for these scenarios, we explored SymAE’s unsupervised potential using a simplified spatial grouping approach on readily available hyperspectral data. This approach assumes spatial correlation in the reflectance information, with nearby pixels likely belonging to the same class. We partitioned the KSC scene into small  $3 \times 3$  pixel groups for SymAE training. We visualized the feature representations using t-SNE plots, as shown in Figure 16. This figure compares the separability of classes in three scenarios: raw spectral data, features learned through ground-truth based grouping, and features learned through our unsupervised  $3 \times 3$  spatial grouping approach.

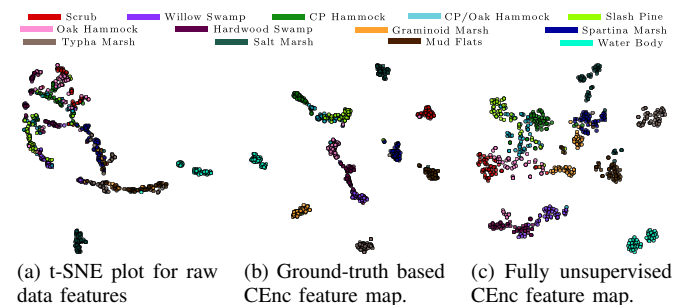


Fig. 16. t-SNE visualization on the KSC dataset. All samples are from the test set of ground-truth based a priori grouping experiments. (a) Raw spectra t-SNE feature map. (b) The same pixels show much better separability in the t-SNE plot of features learned using ground-truth label-based grouping. (c) In the fully unsupervised approach, where pixels are grouped based on spatial proximity ( $3 \times 3$  window), the feature representation shows an overall better separation compared to the raw data feature map, while not as good as ground-truth based grouping.

We repeated the pairwise K-means clustering experiment as described in subsection IV-D for this case and observed an average improvement of 8.7% when using coherent features. Notably, no such improvement was observed when spectra were randomly grouped within the scene, underscoring the importance of meaningful grouping. The clustering analysis, illustrated in Figure 17, offers insights into SymAE’s performance across pairwise classes. We observe performance variations across different classes, with evidence of degradation in certain cases compared to raw spectra. While we cannot be certain without ground truth, these differences might be



attributed to variations in spatial contiguity or extent of the underlying classes. Regions showing apparent performance degradation are perhaps due to the presence of classes that are not spatially contiguous or have a small spatial extent, which could challenge our spatial grouping assumption.

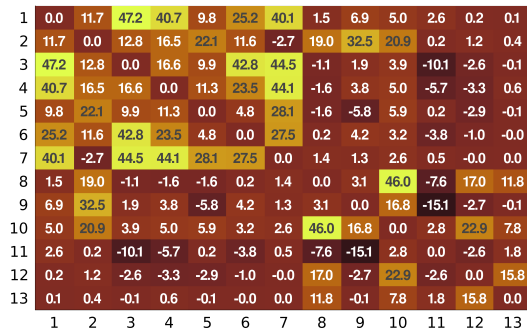


Fig. 17. Heatmap illustrating the improvement in K-means clustering achieved by utilizing the latent coherent code in place of raw spectra, similar to Fig. 8, but without relying on ground truth labels. The heatmap highlights substantial performance enhancements across most classes, while also indicating instances of performance decline among specific class pairs.

To further explore this unsupervised approach, we conducted a focused test on a small patch of the IP dataset, where our spatial-proximity assumption would likely hold. The patch primarily contains two nearby classes: Soybean-clean and Corn-min-till.

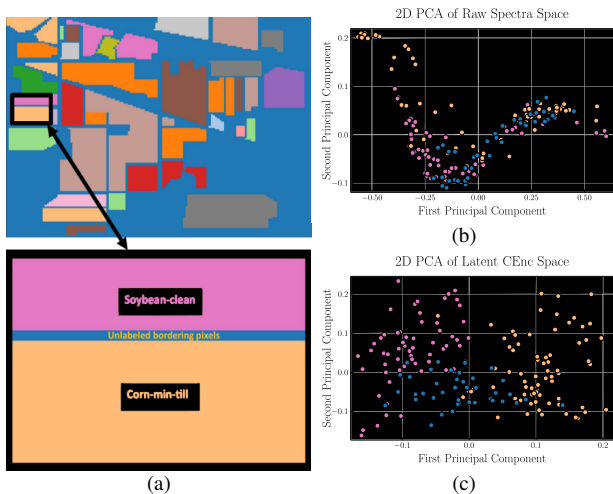


Fig. 18. A focused testing of SymAE without ground truth in IP scene. (a) A selected sub-region within the scene characterized by favorable spatial conditions to test SymAE without ground truth. (b) A 2D representation of the raw spectral space, utilizing the same color scheme as in (a) to visualize data points. (c) The 2D latent space of the coherent code. Pixels near class boundaries pose challenges for differentiation, aligning with our spatial proximity assumption that groups border-adjacent pixels together. However, pixels farther from class boundaries exhibit clear separation within this space, aiding straightforward discrimination.

In line with our prior observations from subsection IV-D, the initial representation of raw spectral data using the first two principal components does not reveal clear class separations. However, a significant improvement in the latent coherent code space, where class distinctions become much more apparent. Notably, pixels located near or along class boundaries remain

challenging to differentiate. This is consistent with the assumption of spatial proximity used during SymAE training, where border-adjacent pixels are grouped together, even if they belong to different classes. On the other hand, pixels farther from these boundaries exhibit clearer separation in the latent space, facilitating their classification with simpler decision boundaries. These preliminary results, based on a basic spatial grouping strategy, indicate that SymAE has potential utility in unsupervised settings. The observed improvement in clustering performance for well-separated regions suggests that SymAE can extract features that support unsupervised analysis. Challenges persist near class boundaries and in areas of high heterogeneity, but these findings provide a foundation for future work in unsupervised feature extraction. Refining grouping techniques could further enhance SymAE’s ability to extract coherent features from complex, unlabeled remote sensing data, especially in scenarios where natural groupings exist but labeled data is scarce.

### B. Scope for Improvement and Future Directions

While the proposed SymAE architecture demonstrates promising results in coherent feature extraction for hyperspectral image classification, we have identified some avenues for improvement and future research directions:

- **Training Efficiency:** For the configurations employed in this study (see IV-A), the SymAE architecture required a substantial training duration, typically taking 6 to 8 hours to complete 3000 to 4000 epochs. While no definitive stopping criterion was established, we consistently observed that the extended training periods led to high discriminative performance of the extracted coherent features. Future research could investigate more efficient disentanglement mechanisms to accelerate this process, potentially reducing the computational overhead while preserving or even enhancing the quality of the learned features.
- **Interpretability of Virtual Spectra:** The current approach does not explicitly enforce physically meaningful transformations in the generation of virtual spectra. Future research could investigate a variational version of SymAE, potentially offering better control over the latent space. This could lead to more interpretable virtual spectra and enable the generation of synthetic spectra with physical significance. Such a generative model could potentially enable tasks such as data augmentation and the exploration of novel spectral scenarios, expanding the utility of the approach beyond feature extraction.
- **Integration with Spectral-Spatial Methods:** While our experiments demonstrated that coherent features can complement some leading spectral-spatial methods, the direct replacement of the hyperspectral cube with a coherent feature cube was somewhat ad hoc. Spectral-spatial methods are typically designed to operate on raw hyperspectral input and often leverage correlations between nearby spectral bands. Our approach does not explicitly enforce such constraints on the coherent features. As a result, directly inputting coherent features may not be the most

effective way to enhance all spectral-spatial methods. Future work could explore designing more structured ways to incorporate permutation-invariant representations alongside spatial contextual information.

- Application to Practical Tasks: Our experiments with purely spectral classification suggest that the coherent features extracted by SymAE possess high discriminative power. This characteristic could be further investigated in practical tasks where spectral features are crucial, such as sub-pixel target detection, material identification, and mineral mapping. Future work could focus on validating the effectiveness of these features in real-world remote sensing applications, potentially revealing new strengths or limitations of the approach in diverse operational scenarios.

## VII. CONCLUSION

Mining robust spectral features is valuable for accurate land cover and material identification in hyperspectral imagery. This article proposes SymAE in the context of HSI, an approach for extracting class-invariant coherent features from hyperspectral data. These coherent features demonstrate improved robustness against spectral variability, contributing to the ongoing efforts to enhance hyperspectral image classification. Experiments across five HSI datasets show that coherent features can be used to achieve state-of-the-art performance in purely spectral pixel-based classification. Furthermore, these features complement leading spectral-spatial methods, enhancing their performance particularly when training and test sets are geographically disjoint. This suggests improved generalization to unseen regions, crucial for practical remote sensing applications. SymAE enables virtual spectra generation through latent space manipulations, offering additional analytical capabilities. Potential future work includes developing a variational SymAE for improved interpretability of virtual spectra and latent space control, exploring applications in scenarios with natural groupings but lacking labels, and expediting the disentanglement process to reduce computational time.

## VIII. ACKNOWLEDGEMENTS

AB and PB are grateful to Indian Space Research Organization (ISRO), specifically their Chandrayaan-2 (AO) program, for the financial support. The authors also wish to disclose the use of AI language models, specifically ChatGPT (developed by OpenAI) and Claude (developed by Anthropic), as assistive tools in refining and editing portions of the manuscript.

### Code Availability

Julia-Flux and Python-PyTorch implementations for training SymAE are available on GitHub<sup>4</sup>. Additionally, the datasets used along with the train-test distributions have been provided.

## REFERENCES

- [1] H Cetin, JT Pafford, and TG Mueller, "Precision agriculture using hyperspectral remote sensing and gis," in *Proceedings of 2nd International Conference on Recent Advances in Space Technologies, 2005. RAST 2005*. IEEE, 2005, pp. 70–77.
- [2] Liang Liang, Liping Di, Lianpeng Zhang, Meixia Deng, Zhihao Qin, Shuhe Zhao, and Hui Lin, "Estimation of crop lai using hyperspectral vegetation indices and a hybrid inversion method," *Remote Sensing of Environment*, vol. 165, pp. 123–134, 2015.
- [3] Enton Bedini, "The use of hyperspectral remote sensing for mineral exploration: A review," *Journal of Hyperspectral Remote Sensing*, vol. 7, no. 4, pp. 189–211, 2017.
- [4] P Debba, FJA Van Ruitenbeek, FD Van Der Meer, EJM Carranza, and A Stein, "Optimal field sampling for targeting minerals using hyperspectral data," *Remote Sensing of Environment*, vol. 99, no. 4, pp. 373–386, 2005.
- [5] James Theiler, Amanda Ziemann, Stefania Matteoli, and Marco Diani, "Spectral variability of remotely sensed target materials: Causes, models, and strategies for mitigation and robust exploitation," *IEEE Geoscience and Remote Sensing Magazine*, vol. 7, no. 2, pp. 8–30, 2019.
- [6] José M Bioucas-Dias, Antonio Plaza, Gustavo Camps-Valls, Paul Scheunders, Nasser Nasrabadi, and Jocelyn Chanussot, "Hyperspectral remote sensing data analysis and future challenges," *IEEE Geoscience and remote sensing magazine*, vol. 1, no. 2, pp. 18–30, 2013.
- [7] Gary A Shaw and Hsiaohua K Burke, "Spectral imaging for remote sensing," *Lincoln laboratory journal*, vol. 14, no. 1, pp. 3–28, 2003.
- [8] Tian Han and David G Goodenough, "Investigation of nonlinearity in hyperspectral imagery using surrogate data methods," *IEEE Transactions on Geoscience and Remote Sensing*, vol. 46, no. 10, pp. 2840–2847, 2008.
- [9] Mark A. Kramer, "Nonlinear principal component analysis using autoassociative neural networks," *AICHe Journal*, vol. 37, no. 2, pp. 233–243, 1991.
- [10] I Goodfellow, Y Bengio, and A Courville, *Deep learning*. MIT Press, 2016.
- [11] Pawan Bharadwaj, Matthew Li, and Laurent Demanet, "Redatuming physical systems using symmetric autoencoders," *Physical Review Research*, vol. 4, no. 2, pp. 023118, 2022.
- [12] Behnood Rasti, Danfeng Hong, Renlong Hang, Pedram Ghamisi, Xudong Kang, Jocelyn Chanussot, and Jon Atli Benediktsson, "Feature extraction for hyperspectral imagery: The evolution from shallow to deep: Overview and toolbox," *IEEE Geoscience and Remote Sensing Magazine*, vol. 8, no. 4, pp. 60–88, 2020.
- [13] Craig Rodarmel and Jie Shan, "Principal component analysis for hyperspectral image classification," *Surveying and Land Information Science*, vol. 62, no. 2, pp. 115–122, 2002.
- [14] Jing Wang and Chein-I Chang, "Independent component analysis-based dimensionality reduction with applications in hyperspectral image analysis," *IEEE transactions on geoscience and remote sensing*, vol. 44, no. 6, pp. 1586–1600, 2006.
- [15] Tatyana V Bandos, Lorenzo Bruzzone, and Gustavo Camps-Valls, "Classification of hyperspectral images with regularized linear discriminant analysis," *IEEE Transactions on Geoscience and Remote Sensing*, vol. 47, no. 3, pp. 862–873, 2009.
- [16] Farid Melgani and Lorenzo Bruzzone, "Classification of hyperspectral remote sensing images with support vector machines," *IEEE Transactions on geoscience and remote sensing*, vol. 42, no. 8, pp. 1778–1790, 2004.
- [17] Dalton Lunga, Saurabh Prasad, Melba M Crawford, and Okan Ersoy, "Manifold-learning-based feature extraction for classification of hyperspectral data: A review of advances in manifold learning," *IEEE Signal Processing Magazine*, vol. 31, no. 1, pp. 55–66, 2013.
- [18] Mathieu Fauvel, Jocelyn Chanussot, and Jon Atli Benediktsson, "Kernel principal component analysis for the classification of hyperspectral remote sensing data over urban areas," *EURASIP Journal on Advances in Signal Processing*, vol. 2009, pp. 1–14, 2009.
- [19] Jón Atli Benediktsson, Jón Aevor Palmason, and Johannes R Sveinsson, "Classification of hyperspectral data from urban areas based on extended morphological profiles," *IEEE Transactions on Geoscience and Remote Sensing*, vol. 43, no. 3, pp. 480–491, 2005.
- [20] Gustavo Camps-Valls, Luis Gomez-Chova, Jordi Muñoz-Marí, Joan Vila-Francés, and Javier Calpe-Maravilla, "Composite kernels for hyperspectral image classification," *IEEE geoscience and remote sensing letters*, vol. 3, no. 1, pp. 93–97, 2006.
- [21] Shutao Li, Weiwei Song, Leyuan Fang, Yushi Chen, Pedram Ghamisi, and Jon Atli Benediktsson, "Deep learning for hyperspectral image classification: An overview," *IEEE Transactions on Geoscience and Remote Sensing*, vol. 57, no. 9, pp. 6690–6709, 2019.
- [22] Wei Hu, Yangyu Huang, Li Wei, Fan Zhang, and Hengchao Li, "Deep convolutional neural networks for hyperspectral image classification," *Journal of Sensors*, vol. 2015, no. 1, pp. 258619, 2015.

- [23] Yushi Chen, Zhouhan Lin, Xing Zhao, Gang Wang, and Yanfeng Gu, "Deep learning-based classification of hyperspectral data," *IEEE Journal of Selected topics in applied earth observations and remote sensing*, vol. 7, no. 6, pp. 2094–2107, 2014.
- [24] Lichao Mou, Pedram Ghamisi, and Xiao Xiang Zhu, "Deep recurrent neural networks for hyperspectral image classification," *IEEE transactions on geoscience and remote sensing*, vol. 55, no. 7, pp. 3639–3655, 2017.
- [25] Renlong Hang, Qingshan Liu, Danfeng Hong, and Pedram Ghamisi, "Cascaded recurrent neural networks for hyperspectral image classification," *IEEE Transactions on Geoscience and Remote Sensing*, vol. 57, no. 8, pp. 5384–5394, 2019.
- [26] Danfeng Hong, Lianru Gao, Jing Yao, Bing Zhang, Antonio Plaza, and Jocelyn Chanussot, "Graph convolutional networks for hyperspectral image classification," *IEEE Transactions on Geoscience and Remote Sensing*, vol. 59, no. 7, pp. 5966–5978, 2020.
- [27] Alexey Dosovitskiy, Lucas Beyer, Alexander Kolesnikov, Dirk Weissenborn, Xiaohua Zhai, Thomas Unterthiner, Mostafa Dehghani, Matthias Minderer, Georg Heigold, Sylvain Gelly, et al., "An image is worth 16x16 words: Transformers for image recognition at scale," *arXiv preprint arXiv:2010.11929*, 2020.
- [28] Danfeng Hong, Zhu Han, Jing Yao, Lianru Gao, Bing Zhang, Antonio Plaza, and Jocelyn Chanussot, "Spectralformer: Rethinking hyperspectral image classification with transformers," *IEEE Transactions on Geoscience and Remote Sensing*, vol. 60, pp. 1–15, 2021.
- [29] Ashish Vaswani, Noam Shazeer, Niki Parmar, Jakob Uszkoreit, Llion Jones, Aidan N Gomez, Lukasz Kaiser, and Illia Polosukhin, "Attention is all you need," *Advances in neural information processing systems*, vol. 30, 2017.
- [30] Zilong Zhong, Jonathan Li, Zhiming Luo, and Michael Chapman, "Spectral-spatial residual network for hyperspectral image classification: A 3-d deep learning framework," *IEEE Transactions on Geoscience and Remote Sensing*, vol. 56, no. 2, pp. 847–858, 2017.
- [31] Zilong Zhong, Ying Li, Lingfei Ma, Jonathan Li, and Wei-Shi Zheng, "Spectral-spatial transformer network for hyperspectral image classification: A factorized architecture search framework," *IEEE Transactions on Geoscience and Remote Sensing*, vol. 60, pp. 1–15, 2021.
- [32] Xuming Zhang, Genyun Sun, Xiuping Jia, Lixin Wu, Aizhu Zhang, Jinchang Ren, Hang Fu, and Yanjuan Yao, "Spectral-spatial self-attention networks for hyperspectral image classification," *IEEE Transactions on Geoscience and Remote Sensing*, vol. 60, pp. 1–15, 2022.
- [33] Swalpa Kumar Roy, Suvjit Manna, Tiecheng Song, and Lorenzo Bruzzone, "Attention-based adaptive spectral-spatial kernel resnet for hyperspectral image classification," *IEEE Transactions on Geoscience and Remote Sensing*, vol. 59, no. 9, pp. 7831–7843, 2020.
- [34] Di Wang, Bo Du, and Liangpei Zhang, "Fully contextual network for hyperspectral scene parsing," *IEEE Transactions on Geoscience and Remote Sensing*, vol. 60, pp. 1–16, 2021.
- [35] Le Sun, Guangrui Zhao, Yuhui Zheng, and Zebin Wu, "Spectral-spatial feature tokenization transformer for hyperspectral image classification," *IEEE Transactions on Geoscience and Remote Sensing*, vol. 60, pp. 1–14, 2022.
- [36] Renlong Hang, Zhu Li, Qingshan Liu, Pedram Ghamisi, and Shuvra S. Bhattacharyya, "Hyperspectral image classification with attention-aided cnns," *IEEE Transactions on Geoscience and Remote Sensing*, vol. 59, no. 3, pp. 2281–2293, 2021.
- [37] Bing Liu, Yifan Sun, Anzhu Yu, Zhixiang Xue, and Xibing Zuo, "Hyperspectral meets optical flow: Spectral flow extraction for hyperspectral image classification," *IEEE Transactions on Image Processing*, 2023.
- [38] Mingsong Li, Yikun Liu, Guangkuo Xue, Yuwen Huang, and Gongping Yang, "Exploring the relationship between center and neighborhoods: Central vector oriented self-similarity network for hyperspectral image classification," *IEEE Transactions on Circuits and Systems for Video Technology*, vol. 33, no. 4, pp. 1979–1993, 2022.
- [39] Mingsong Li, Wei Li, Yikun Liu, Yuwen Huang, and Gongping Yang, "Adaptive mask sampling and manifold to euclidean subspace learning with distance covariance representation for hyperspectral image classification," *IEEE Transactions on Geoscience and Remote Sensing*, vol. 61, pp. 1–18, 2023.
- [40] Gregg Vane, Robert O Green, Thomas G Chrien, Harry T Enmark, Earl G Hansen, and Wallace M Porter, "The airborne visible/infrared imaging spectrometer (aviris)," *Remote sensing of environment*, vol. 44, no. 2-3, pp. 127–143, 1993.
- [41] B Kunkel, Fritz Blechinger, R Lutz, R Doerffer, Heinz Van Der Piepen, and M Schroder, "Rosis (reflective optics system imaging spectrometer)-a candidate instrument for polar platform missions," in *Optoelectronic technologies for remote sensing from space*. SPIE, 1988, vol. 868, pp. 134–141.
- [42] Wim A Mulder, "Rigorous redatuming," *Geophysical Journal International*, vol. 161, no. 2, pp. 401–415, 2005.
- [43] John R Berryhill, "Wave-equation datuming," *Geophysics*, vol. 44, no. 8, pp. 1329–1344, 1979.
- [44] Manzil Zaheer, Satwik Kottur, Siamak Ravanbakhsh, Barnabás Póczos, Ruslan Salakhutdinov, and Alexander J. Smola, "Deep sets," *Advances in Neural Information Processing Systems*, , no. ii, pp. 3392–3402, apr 2017.
- [45] Nitish Srivastava, Geoffrey Hinton, Alex Krizhevsky, Ilya Sutskever, and Ruslan Salakhutdinov, "Dropout: a simple way to prevent neural networks from overfitting," *The journal of machine learning research*, vol. 15, no. 1, pp. 1929–1958, 2014.
- [46] Steven M Adler-Golden, Michael W Matthew, Lawrence S Bernstein, Robert Y Levine, Alexander Berk, Steven C Richtsmeier, Prabhat K Acharya, Gail P Anderson, Jerry W Felde, JA Gardner, et al., "Atmospheric correction for shortwave spectral imagery based on modtran4," in *Imaging Spectrometry V*. International Society for Optics and Photonics, 1999, vol. 3753, pp. 61–69.
- [47] Michael Innes, Elliot Saba, Keno Fischer, Dhairya Gandhi, Marco Conetto Rudilosso, Neethu Mariya Joy, Tejan Karmali, Avik Pal, and Viral Shah, "Fashionable modelling with flux," *CoRR*, vol. abs/1811.01457, 2018.
- [48] Nirmal Keshava and John F Mustard, "Spectral unmixing," *IEEE signal processing magazine*, vol. 19, no. 1, pp. 44–57, 2002.
- [49] Rob Heylen, Mario Parente, and Paul Gader, "A review of nonlinear hyperspectral unmixing methods," *IEEE Journal of Selected Topics in Applied Earth Observations and Remote Sensing*, vol. 7, no. 6, pp. 1844–1868, 2014.
- [50] Burkni Palsson, Johannes R Sveinsson, and Magnus O Ulfarsson, "Blind hyperspectral unmixing using autoencoders: A critical comparison," *IEEE Journal of Selected Topics in Applied Earth Observations and Remote Sensing*, vol. 15, pp. 1340–1372, 2022.
- [51] Behnood Rasti, Paul Scheunders, Pedram Ghamisi, Giorgio Licciardi, and Jocelyn Chanussot, "Noise reduction in hyperspectral imagery: Overview and application," *Remote Sensing*, vol. 10, no. 3, pp. 482, 2018.
- [52] Pascal Vincent, Hugo Larochelle, Yoshua Bengio, and Pierre-Antoine Manzagol, "Extracting and composing robust features with denoising autoencoders," in *Proceedings of the 25th international conference on Machine learning*, 2008, pp. 1096–1103.
- [53] Chen Xing, Li Ma, Xiaoquan Yang, et al., "Stacked denoise autoencoder based feature extraction and classification for hyperspectral images," *Journal of Sensors*, vol. 2016, 2016.
- [54] Marian-Daniel Iordache, José M Bioucas-Dias, and Antonio Plaza, "Hyperspectral unmixing with sparse group lasso," in *2011 IEEE International Geoscience and Remote Sensing Symposium*. IEEE, 2011, pp. 3586–3589.
- [55] Tianqi Chen and Carlos Guestrin, "Xgboost: A scalable tree boosting system," in *Proceedings of the 22nd acm sigkdd international conference on knowledge discovery and data mining*, 2016, pp. 785–794.
- [56] Chunbo Cheng, Hong Li, Jiangtao Peng, Wenjing Cui, and Liming Zhang, "Hyperspectral image classification via spectral-spatial random patches network," *IEEE Journal of Selected Topics in Applied Earth Observations and Remote Sensing*, vol. 14, pp. 4753–4764, 2021.
- [57] Swalpa Kumar Roy, Ankur Deria, Chiranjibi Shah, Juan M Haut, Qian Du, and Antonio Plaza, "Spectral-spatial morphological attention transformer for hyperspectral image classification," *IEEE Transactions on Geoscience and Remote Sensing*, vol. 61, pp. 1–15, 2023.
- [58] Yifan Sun, Bing Liu, Xuchu Yu, Anzhu Yu, Kuiliang Gao, and Lei Ding, "Perceiving spectral variation: Unsupervised spectrum motion feature learning for hyperspectral image classification," *IEEE Transactions on Geoscience and Remote Sensing*, vol. 60, pp. 1–17, 2022.
- [59] Shuo Wang, Zhengjun Liu, Yiming Chen, Chengchao Hou, Aixia Liu, and Zhenbei Zhang, "Expansion spectral-spatial attention network for hyperspectral image classification," *IEEE Journal of Selected Topics in Applied Earth Observations and Remote Sensing*, vol. 16, pp. 6411–6427, 2023.